

# Dynamical model for pion photo-production reactions on the deuteron and the extraction of neutron-target observables

S. X. Nakamura,<sup>1</sup> H. Kamano,<sup>2,3,4</sup> T.-S. H. Lee,<sup>5</sup> and T. Sato<sup>3,4,6</sup>

<sup>1</sup>*Laboratório de Física Teórica e Computacional - LFTC,*

*Universidade Cruzeiro do Sul, São Paulo, SP 01506-000, Brazil*

<sup>2</sup>*KEK Theory Center, Institute of Particle and Nuclear Studies (IPNS),  
High Energy Accelerator Research Organization (KEK), Tsukuba, Ibaraki 305-0801, Japan*

<sup>3</sup>*J-PARC Branch, KEK Theory Center,  
IPNS, KEK, Tokai, Ibaraki 319-1106, Japan*

<sup>4</sup>*Research Center for Nuclear Physics,  
Osaka University, Ibaraki, Osaka 567-0047, Japan*

<sup>5</sup>*Physics Division, Argonne National Laboratory, Argonne, Illinois 60439, USA*

<sup>6</sup>*Department of Physics, Osaka University, Toyonaka, Osaka 560-0043, Japan*

## Abstract

Within the multiple scattering formulation, we predict the cross sections of  $d(\gamma, \pi)NN$  by using a dynamical model of  $\pi N$  and  $\gamma N$  reactions in the nucleon resonance region. The calculations include the impulse term and the final-state interaction (FSI) terms due to pion-exchange and nucleon-exchange. We show that the off-shell effects, calculated from the meson-exchange mechanisms, on the propagations of the exchanged nucleon and pion are significant in determining the reaction amplitudes. The FSI effects on the predicted cross sections are found to be important at energies near the  $\Delta(1232)$  resonance, and are still significant at higher energies. The results are in good agreement with most of the available data of  $d(\gamma, \pi^0)np$  and  $d(\gamma, \pi^-)pp$  reactions. We use our predictions to examine a commonly used procedure for extracting the (un)polarized  $\gamma n \rightarrow \pi N$  observables from the  $d(\gamma, \pi)NN$  data. It is demonstrated that the extracted  $\gamma n \rightarrow \pi N$  unpolarized cross sections still contain the FSI effects even after the kinematical cuts are applied to isolate the quasi-free events. However the same procedure works well for the polarization observables  $\Sigma$ ,  $E$ , and  $G$ . We also find that the FSI effects on the determinations of the cross sections of  $\gamma n \rightarrow \pi^0 n$  can be somewhat different from those of  $\gamma p \rightarrow \pi^0 p$ . We point out the importance of applying a cut on the final  $\pi N$  invariant mass to efficiently suppress a problematic Fermi smearing effect, thereby maintaining a good accuracy of the extraction. An experiment-theory iteration procedure for extracting the observables of  $\gamma n \rightarrow \pi N$  from the  $d(\gamma, \pi)NN$  data is suggested.

PACS numbers: 11.80.La, 13.60.Le, 13.88.+e, 14.20.Gk

## I. INTRODUCTION

The developments of dynamical models for  $\pi N$  and  $\gamma N$  reactions were motivated by the success of the meson-exchange models [1] for the  $NN$  interactions and the earlier attempts [2] to relate the isobar models of nucleon resonances to the predictions of constituent quark models [3]. Within the formulation given in Refs. [4, 5], the development of dynamical models of  $\pi N$  and  $\gamma N$  reactions has two main objectives:

1. Develop interpretations of the nucleon resonances ( $N^*$ ) within the framework that the excitations of the nucleon can be described in terms of bare baryon states and meson-exchange interactions. With the parameters determined by fitting the data of  $\pi N$  and  $\gamma N$  reactions up to the invariant mass  $W = 2$  GeV, the poles and residues of nucleon resonances are extracted by performing analytic continuations of the partial-wave amplitudes predicted within the constructed model to the complex energy-plane.
2. Apply the constructed dynamical model to investigate the propagations of mesons and nucleon resonances in nuclei, which are crucial for analyzing data from experiments on nuclear targets in the nucleon resonance region, such as the recent experiments on the neutrino oscillations [6].

With the efforts reported in Refs. [7–19], we have achieved the first objective. In this paper, we will take a step toward reaching the second objective by applying the constructed dynamical coupled-channel model (ANL-Osaka model) presented in Ref. [18, 19] to investigate pion photo-production on the simplest nucleus, the deuteron ( $d$ ). We will focus on the  $d(\gamma, \pi)NN$  reactions for two reasons:

1. An uncertainty in the construction of the ANL-Osaka model was in the determination of the isospin structure of the nucleon resonances by fitting the available data of  $\gamma n \rightarrow \pi^- p$  which were extracted from the  $d(\gamma, \pi^-)pp$  data with some procedures to select the  $\gamma n \rightarrow \pi^- p$  events. Furthermore,  $\gamma n \rightarrow \pi^0 n$  data included in our previous fit were rather scarce.<sup>1</sup> We therefore need to examine whether our predictions of  $d(\gamma, \pi)NN$  will be in agreement with the original data of  $d(\gamma, \pi^-)pp$  and  $d(\gamma, \pi^0)pn$ .
2. The extractions of  $\gamma n \rightarrow \pi^- p$ ,  $\pi^0 n$  cross sections from the data of  $d(\gamma, \pi^-)pp$  and  $d(\gamma, \pi^0)pn$  are important tasks at Jefferson Laboratory (JLab) [20–23] and Mainz [24–28]. It is therefore interesting to use our predictions to examine the extent to which their procedures are consistent with a dynamical model approach which has significant differences with the previous approaches [29, 30].

One of the important features of the ANL-Osaka model is that the amplitudes are generated from an energy *independent* Hamiltonian which can be included in the conventional Hamiltonian formulation for developing many-body descriptions of nuclear reactions. This is achieved by using a unitary transformation method [4, 31] to derive hadron-hadron interactions from relativistic quantum field theory with meson and baryon degrees of freedom. This feature allows us to use rigorously the well-established multiple-scattering formulation [32] to develop a reaction model for  $d(\gamma, \pi)NN$  reactions. For our limited purpose here, we follow

---

<sup>1</sup> For determining the isospin structure of nucleon resonances,  $\gamma p \rightarrow \pi^0 p, \pi^+ n$  data and either of  $\gamma n \rightarrow \pi^- p$  or  $\gamma n \rightarrow \pi^0 n$  data are needed in the fit if the data are of very high accuracy. This is however not the case, thus the fits including both of the neutron data may be needed to reduce the uncertainty.

the previous investigations [29, 30, 33–37] to only include the single scattering (impulse) amplitudes and the double scattering amplitudes due to pion-exchange and nucleon-exchange mechanisms. The exchanges of unstable particles  $\rho$ ,  $\sigma$  and  $\Delta(1232)$ , which can be generated from the ANL-Osaka model, are more difficult to calculate and are neglected in this work for simplicity.

Thus our task is to develop formula for calculating the amplitudes illustrated in Fig. 1. The  $\gamma N \rightarrow \pi N$  and  $\pi N \rightarrow \pi N$  amplitudes for evaluating the pion re-scattering term of Fig. 1(c) can be generated from the ANL-Osaka model. The initial deuteron wave function and the  $NN \rightarrow NN$  amplitudes in Fig. 1(b) can be generated from any of the available high-precision  $NN$  potentials. To be consistent with the meson-exchange mechanisms of the ANL-Osaka model, we choose the CD-Bonn potential [38]. There are two important issues in practical calculations of the matrix elements of these mechanisms, as discussed well in the earlier investigations [39, 40] of the multiple scattering of hadrons from nuclei within the Hamiltonian formulation. First, we need to define a Lorentz boost transformation to relate the  $\gamma N \rightarrow \pi N$ ,  $\pi N \rightarrow \pi N$  and  $NN \rightarrow NN$  amplitudes in Fig. 1 in the photon-deuteron laboratory frame to those in the two-body center of mass (CM) frame where the two-body amplitudes are generated from Hamiltonian by solving scattering equations in partial-wave representation. In particular, the spin rotations must be taken into account relativistically for investigating polarization observables. Here we follow the method of relativistic quantum mechanics, as detailed in Ref. [41–43]. The second issue is that the resulting FSI amplitudes will include loop-integrations over the off-energy-shell matrix elements of the two-body amplitudes in Fig. 1. Thus it is necessary to introduce an approximation to choose the collision energies in generating these two-body off-shell matrix elements. Here we will use an approach which accounts for the energy shared by the spectator nucleon and pion in Fig. 1.

A commonly used procedure of extracting cross sections for the neutron target from data on the deuteron is to apply a certain set of kinematical cuts to the deuteron data and assume that the selected events are from the quasi-free processes on a single nucleon. However, this procedure has been always with a concern that the rescattering effects, as illustrated in Fig. 1, can still be in the selected events and must be accounted for in the extraction. This has been addressed in recent years in Refs. [20, 29, 30] within a model using the two-body amplitudes generated from the SAID model [44]. Here we will also investigate this problem by using our model with the mechanisms illustrated in Fig. 1. The mechanisms considered in Refs. [20, 29] for  $d(\gamma, \pi^-)pp$  are the same as those illustrated in Fig. 1, while the pion-exchange mechanism [Fig. 1(c)] is not considered in Ref. [30] for  $d(\gamma, \pi^0)pn$ . Furthermore our approach has significant differences with Refs. [20, 29, 30] in the formulation of the  $d(\gamma, \pi)NN$  reaction and the calculations. In particular, the off-shell propagations of pions and nucleons are treated rather differently.

Within our model, we develop explicit formulas, which can account for the kinematical cuts recently employed by the experimental groups, to predict  $d(\gamma, \pi)NN$  cross sections. The predicted results are taken as ‘data’ to extract the  $\gamma n \rightarrow \pi N$  observables which are then compared with those on a free neutron calculated from the ANL-Osaka model. The differences in the comparison determine the extent to which the FSI have been removed, or some artifacts have been introduced, by using the kinematical cuts to extract the  $\gamma n \rightarrow \pi N$  observables. We will examine the differences with the investigations of Refs. [29, 30] in extracting the unpolarized differential cross sections. Meanwhile, no theoretical study with a photon-deuteron reaction model as ours has been done on the extraction of polarization observables for  $\gamma n \rightarrow \pi N$  of the current interests [22, 28]; we will conduct such a study for

the first time.

The organization of the rest of this paper is as follows. In Sec. II, we present formulas for calculating the amplitudes of the impulse term [Fig. 1.(a)], nucleon re-scattering ( $N$ -exchange) term [Fig. 1.(b)], and pion re-scattering ( $\pi$ -exchange) term [Fig. 1.(c)]. The results for comparing our predictions with the available data of  $d(\gamma, \pi^0)pn$  and  $d(\gamma, \pi^0)pp$ , and for examining the importance of FSI and off-shell effects will be given in Sec. III. In Sec. IV, we examine within our model the extent to which the procedure using kinematical cuts to extract  $\gamma n \rightarrow \pi^0 n, \pi^- p$  from the data of  $d(\gamma, \pi)NN$  can be justified. The discussions on future possible developments are given in Sec. V.

## II. FORMULATION

In this section, we describe the theoretical formulation used in our investigation of  $d(\gamma, \pi)NN$  reactions. All of the formulas for calculations are presented with the normalizations:  $\langle \mathbf{k}' | \mathbf{k} \rangle = \delta^{(3)}(\mathbf{k}' - \mathbf{k})$  for plane-wave states and  $\langle \Phi_d | \Phi_d \rangle = 1$  for bound states.

### A. Model Hamiltonian with meson and baryon degrees of freedom

Our starting point is the following many-body Hamiltonian

$$H = H_0 + \frac{1}{2} \sum_{i \neq j} V_{NN,NN}(i, j) + \sum_i h_{\text{AO}}^I(i), \quad (1)$$

where  $H_0$  is the free Hamiltonian for all particles in the considered processes,  $V_{NN,NN}(i, j)$  is a nucleon-nucleon potential between the nucleons  $i$  and  $j$ , and

$$h_{\text{AO}}^I(i) = \sum_{c, c'} v_{c, c'}(i) + \sum_{N^*} \sum_c [\Gamma_{N^*, c}(i) + \Gamma_{N^*, c}^\dagger(i)], \quad (2)$$

is the interaction Hamiltonian of the ANL-Osaka (AO) model. The channels included are  $c, c' = \gamma N, \pi N, \eta N, K\Lambda, K\Sigma$  and  $\pi\pi N$  with resonant  $\pi\Delta, \rho N$ , and  $\sigma N$  components. The energy independent meson-exchange potentials  $v_{c, c'}$  are derived from phenomenological Lagrangians by using the unitary transformation method [4, 31]. The vertex interaction  $\Gamma_{N^*, c}$  defines the formation of a bare  $N^*$  state from a channel  $c$ . The parameters of the Hamiltonian  $h_{\text{AO}}^I$  have been determined in Refs. [18, 19] by fitting about 26,000 data points of the  $\pi N$  and  $\gamma N$  reactions up to the invariant mass  $W \simeq 2$  GeV.

Here we mention that the model Hamiltonian defined above is a very significant extension of the Hamiltonian developed in Refs. [45, 46] where only  $\pi$ ,  $N$ , and  $\Delta$  degrees of freedom are included. It can be used to investigate  $\pi$ ,  $\eta$ , and two-pion production reactions on nuclei in the nucleon resonance region. The first attempt in this direction was made to investigate the  $d(\gamma, \eta)pn$  reaction in the context of extracting the low-energy  $\eta N$  scattering parameters [47]. Here we focus on the pion photo-production on the deuteron to test our predictions and to also address the issues concerning the extractions of the observables of the  $\gamma N \rightarrow \pi N$  from the data of  $d(\gamma, \pi)NN$  reactions.

## B. Scattering amplitudes for $d(\gamma, \pi)NN$ reactions

Starting with the scattering  $T$ -matrix given by the Hamiltonian Eq. (1), it is straightforward to follow the well-developed procedures [32] to obtain a multiple scattering formulation of the  $d(\gamma, \pi)NN$  reactions. Following the previous investigations [29, 30, 33, 37], we will only keep the single-scattering (impulse) terms and the double scattering terms with  $\pi NN$  intermediate states. The  $T$ -matrix operator for the  $d(\gamma, \pi)NN$  reactions can then be written as

$$T(E) = \sum_i \tau_{\pi N_i, \gamma N_i}(E) + \sum_{i \neq j} \tau_{N_i N_j, N_i N_j}(E) \frac{|\pi N_i N_j\rangle \langle \pi N_i N_j|}{E - H_0 + i\epsilon} \tau_{\pi N_i, \gamma N_i}(E) \\ + \sum_{i \neq j} \tau_{\pi N_j, \pi N_j}(E) \frac{|\pi N_i N_j\rangle \langle \pi N_i N_j|}{E - H_0 + i\epsilon} \tau_{\pi N_i, \gamma N_i}(E), \quad (3)$$

where  $E$  is the total energy of the  $\gamma d$  system,  $\tau_{\alpha N_i, \beta N_i}(E)$  is a scattering operator associated with the  $i$ -th nucleon in the deuteron. Note that the matrix elements of  $\tau_{\alpha N_i, \beta N_i}(E)$  are determined by the total Hamiltonian Eq. (1) and cannot be calculated exactly. Therefore, we adopt the spectator approximation [39, 40] as

$$\tau_{\alpha, N_i, \beta N_i}(E) \sim t_{\alpha, N_i, \beta N_i}(E - E_{\text{spectator}}), \quad (4)$$

where  $t_{\alpha, N_i, \beta N_i}(E')$  is the two-body scattering operator in free space, and  $E_{\text{spectator}}$  is the energy of the spectator of the two-body scattering in the  $\gamma NN$  or  $\pi NN$  three-particle states, as seen in Fig. 1. The resulting  $T$ -matrix operator is consistent with that of the Faddeev framework up to and including the double scattering terms, as has been also discussed in Ref. [47].

To proceed further, we need to define the matrix elements of the scattering operator  $t_{c, c'}(W)$  with an invariant mass  $W$ . Within the ANL-Osaka model, these matrix elements are generated in the two-body CM frame by solving the following coupled-channel equations in each partial wave:

$$\langle k | t_{c, c'}(W) | k' \rangle = \langle k | V_{c, c'}(W) | k' \rangle \\ + \sum_{c''} \int k''^2 dk'' \frac{\langle k | V_{c, c''}(W) | k'' \rangle \langle k'' | t_{c'', c'}(W) | k' \rangle}{W - E_{c'', 1}(k'') - E_{c'', 2}(k'') - \Sigma_{c''}(k'', W) + i\epsilon}, \quad (5)$$

where  $k$ ,  $k'$  and  $k''$  are the momenta in the CM frame,  $E_{c, i}(k) = \sqrt{m_{c, i}^2 + k^2}$  is the energy of a particle  $i$  in a channel  $c$  with the mass  $m_{c, i}$ ,  $c, c', c'' = \pi N, \eta N, \pi \Delta, \rho N, \sigma N, K \Lambda, K \Sigma$  are the considered channels, and  $c' = \gamma N$  channel is included perturbatively;  $\Sigma_{c''}$  is the self-energy for the unstable channels  $c'' = \pi \Delta, \rho N, \sigma N$ , and is zero for the other stable channels. The driving term is

$$V_{c, c'}(W) = v_{c, c'} + \sum_{N^*} \Gamma_{N^*, c}^\dagger \frac{1}{W - M_{N^*}} \Gamma_{N^*, c'} + Z(W), \quad (6)$$

where  $M_{N^*}$  is the bare mass of an excited nucleon state  $N^*$ ;  $Z(W)$  is a particle-exchange Z-diagram in which a  $\pi \pi N$  channel is included. Note that the initial and final states of each matrix element in Eq. (5) can be on-energy-shell [ $W = E_{c, 1}(k) + E_{c, 2}(k) = E_{c', 1}(k') + E_{c', 2}(k')$ ]

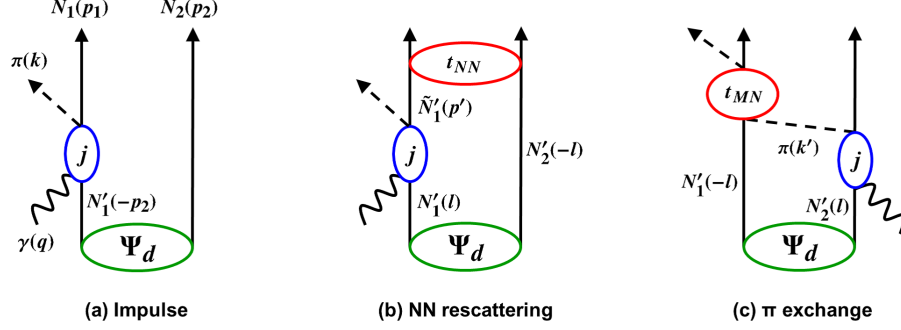


FIG. 1. Diagrammatic representation of reaction mechanisms considered in this work for  $d(\gamma, \pi)NN$ : (left) impulse, (center)  $NN$  rescattering ( $N$ -exchange), (right)  $\pi N$  rescattering ( $\pi$ -exchange) mechanisms.

or off-energy-shell [ $W \neq E_{c,1}(k) + E_{c,2}(k) \neq E_{c',1}(k') + E_{c',2}(k')$ ] within the Hamiltonian formulation.

By using Eqs. (3) and (4) and the momenta defined in Fig. 1, the Lorentz invariant scattering amplitude of  $d(\gamma, \pi)NN$  can then be written as

$$M_{f,i}(E) = \sqrt{\frac{(2E_\pi(\mathbf{k}))E_N(\mathbf{p}_1)E_N(\mathbf{p}_2)}{m_N^2}} \times \left( t_{f,i}^{\text{imp}}(E) + t_{f,i}^{N\text{-exc}}(E) + t_{f,i}^{\pi\text{-exc}}(E) + \{\text{exchange terms}\} \right) \sqrt{(2\omega)(2E_d(\mathbf{p}_d))}, \quad (7)$$

where the sub-indices  $f$  and  $i$  stand for the final state  $\langle \pi(\mathbf{k}, t_\pi) N_1(\mathbf{p}_1, s_1, t_1), N_2(\mathbf{p}_2, s_2, t_2) |$ , and the initial state  $|\gamma(\mathbf{q}, \lambda), \Psi_d(s_d)\rangle$ , respectively,  $\omega = |\mathbf{q}|$  is the photon energy, and for the laboratory frame,

$$t_{f,i}^{\text{imp}} = \sqrt{2} \sum_{s'_1, t'_1} \langle \pi(\mathbf{k}, t_\pi) N_1(\mathbf{p}_1, s_1, t_1) | t_{\pi N, \gamma N}(M_{\pi N_1}) | \gamma(\mathbf{q}, \lambda) N'_1(-\mathbf{p}_2, s'_1, t'_1) \rangle \times \langle N'_1(-\mathbf{p}_2, s'_1, t'_1) N_2(\mathbf{p}_2, s_2, t_2) | \Psi_d(s_d) \rangle, \quad (8)$$

$$t_{f,i}^{N\text{-exc}} = \sqrt{2} \sum_{s'_1, \tilde{s}'_1, s'_2, t'_1} \int d\mathbf{l} \times \langle N_1(\mathbf{p}_1, s_1, t_1) N_2(\mathbf{p}_2, s_2, t_2) | t_{NN, NN}(M_{N_1 N_2}) | \tilde{N}'_1(\mathbf{q} - \mathbf{k} + \mathbf{l}, \tilde{s}'_1, t_1) N'_2(-\mathbf{l}, s'_2, t_2) \rangle \times \frac{\langle \pi(\mathbf{k}, t_\pi) \tilde{N}'_1(\mathbf{q} - \mathbf{k} + \mathbf{l}, \tilde{s}'_1, t_1) | t_{\pi N, \gamma N}(W) | \gamma(\mathbf{q}, \lambda) N'_1(\mathbf{l}, s'_1, t'_1) \rangle}{E - E_N(\mathbf{q} - \mathbf{k} + \mathbf{l}) - E_N(-\mathbf{l}) - E_\pi(\mathbf{k}) + i\epsilon} \times \langle N'_1(\mathbf{l}, s'_1, t'_1) N'_2(-\mathbf{l}, s'_2, t_2) | \Psi_d(s_d) \rangle, \quad (9)$$

$$t_{f,i}^{\pi\text{-exc}} = \sqrt{2} \sum_{s'_1, s'_2, t'_1, t'_2, t'_\pi} \int d\mathbf{l} \langle \pi(\mathbf{k}, t_\pi) N_1(\mathbf{p}_1, s_1, t_1) | t_{\pi N, \pi N}(M_{\pi N_1}) | \pi(\mathbf{q} - \mathbf{p}_2 + \mathbf{l}, t'_\pi) N'_1(-\mathbf{l}, s'_1, t'_1) \rangle \times \frac{\langle \pi(\mathbf{q} - \mathbf{p}_2 + \mathbf{l}, t'_\pi) N_2(\mathbf{p}_2, s_2, t_2) | t_{\pi N, \gamma N}(W) | \gamma(\mathbf{q}, \lambda) N'_2(\mathbf{l}, s'_2, t'_2) \rangle}{E - E_N(\mathbf{p}_2) - E_N(-\mathbf{l}) - E_\pi(\mathbf{q} - \mathbf{p}_2 + \mathbf{l}) + i\epsilon} \times \langle N'_1(-\mathbf{l}, s'_1, t'_1) N'_2(\mathbf{l}, s'_2, t'_2) | \Psi_d(s_d) \rangle. \quad (10)$$

The exchange terms in Eq. (7) can be obtained from Eqs. (8)-(10) by flipping the overall sign and interchanging all subscripts 1 and 2 for the nucleons in the intermediate and final  $\pi NN$  states. Here, the deuteron state with spin projection  $s_d$  is denoted as  $|\Psi_d(s_d)\rangle$ ;  $|N(\mathbf{p}, s, t)\rangle$  the nucleon state with momentum  $\mathbf{p}$  and spin and isospin projections  $s$  and  $t$ ;  $|\gamma(\mathbf{q}, \lambda)\rangle$  the photon state with momentum  $\mathbf{q}$  and polarization  $\lambda$ ;  $|\pi(\mathbf{k}, t_\pi)\rangle$  the pion state with momentum  $\mathbf{k}$  and the isospin projection  $t_\pi$ . The total energy in the laboratory frame,  $E$ , is given by  $E = \omega + m_d$  where  $m_d$  is the deuteron mass. The invariant masses for the matrix elements of the two-body subprocesses are calculated according to the momentum variables specified in Fig. 1 and  $E - E_{\text{spectator}}$  of the spectator approximation defined by Eq. (4):

$$M_{\pi N_1} = \sqrt{[E_\pi(\mathbf{k}) + E_N(\mathbf{p}_1)]^2 - (\mathbf{k} + \mathbf{p}_1)^2}, \quad (11)$$

$$M_{N_1 N_2} = \sqrt{[E_N(\mathbf{p}_1) + E_N(\mathbf{p}_2)]^2 - (\mathbf{p}_1 + \mathbf{p}_2)^2}, \quad (12)$$

$$W = \sqrt{[E - E_N(-\mathbf{l})]^2 - (\mathbf{l} + \mathbf{q})^2}. \quad (13)$$

To be consistent with the chosen CD-Bonn  $NN$  potential [38] for generating the  $NN$  scattering amplitudes and the deuteron bound state, the two-nucleon energy in the propagator of the nucleon re-scattering amplitude  $t_{NN,NN}$  in Eq. (9), is calculated with a non-relativistic approximation

$$E_N(\mathbf{q} - \mathbf{k} + \mathbf{l}) + E_N(-\mathbf{l}) \sim \sqrt{(2m_N)^2 + (\mathbf{q} - \mathbf{k})^2} + \frac{(\mathbf{q}/2 - \mathbf{k}/2 + \mathbf{l})^2}{m_N}. \quad (14)$$

The amplitudes  $\langle \pi N | t_{\pi N, \gamma N} | \gamma N' \rangle$  of the pion photoproduction and  $\langle \pi N | t_{\pi N, \pi N} | \pi' N' \rangle$  of the pion-nucleon scattering in Eqs. (8)-(10) are first generated from the ANL-Osaka model by solving the coupled-channel equation of Eq. (5) in the two-body CM frame. The resulting matrix elements are then boosted to the considered  $\gamma$ -deuteron frame. Here we follow the approach of Ref. [41] based on the instant form of relativistic quantum mechanics [43]. The same frame-transformation procedure is also needed to calculate the matrix element  $\langle NN | t_{NN,NN} | NN \rangle$  of  $NN$  scattering in Eq. (9). The formulas for calculating these matrix elements in the  $\gamma$ -deuteron frame are given in Appendix A.

Here we note an important difference between our dynamical model approach and the approach of Refs. [29, 30]. In the loop-integrations of Eqs. (9) and (10), the two-body matrix elements can be off-energy-shell and are calculated exactly from the ANL-Osaka model and the CD-Bonn potential as explained above. The equations for calculating FSI in Refs. [29, 30] are similar to our expressions, but the two-body matrix elements are taken as their on-shell values and are taken out of the loop-integrations. For  $NN \rightarrow NN$ , they include a monopole form factor of Ref. [35] to account for the off-shell effect. These simplifications greatly reduce the computation task. We will examine the on-shell approximation within our formulation in Sec. III.

### C. Cross section formula

The reaction cross section for  $\gamma(\mathbf{q}) + d(\mathbf{p}_d) \rightarrow \pi(\mathbf{k}) + N_1(\mathbf{p}_1) + N_2(\mathbf{p}_2)$  is defined by

$$d\sigma = \frac{(2\pi)^4}{|\mathbf{v}_{rel}|} \delta^{(3)}(\mathbf{p}_d + \mathbf{q} - \mathbf{p}_1 - \mathbf{p}_2 - \mathbf{k}) \delta(E_d(\mathbf{p}_d) + \omega - E_N(\mathbf{p}_1) - E_N(\mathbf{p}_2) - E_\pi(\mathbf{k})) \\ \times d\mathbf{p}_1 d\mathbf{p}_2 d\mathbf{k} \left[ \frac{m_N}{E_N(\mathbf{p}_1)} \frac{m_N}{E_N(\mathbf{p}_2)} \frac{1}{2E_\pi(\mathbf{k})} \right] |M_{f,i}(E)|^2 \left[ \frac{1}{2E_d(\mathbf{p}_d)} \frac{1}{2\omega} \right], \quad (15)$$

where  $\mathbf{v}_{rel}$  is the relative velocity of the initial  $\gamma$ - $d$  system, and the Lorentz invariant amplitude  $M_{f,i}(E)$  has been defined by Eqs. (7)-(10). The unpolarized differential cross section with respect to the pion emission angle in the laboratory frame ( $\mathbf{p}_d = 0$ ) derived from Eq. (15) can be written as

$$\frac{d\sigma}{d\Omega} \equiv \frac{d\sigma}{d\Omega_{\mathbf{k}}} = \frac{1}{6} \sum_{\lambda, s_d} \frac{d\sigma(\lambda, s_d)}{d\Omega_{\mathbf{k}}}, \quad (16)$$

where  $\lambda$  is the photon polarization,  $s_d$  is the  $z$ -component of the deuteron spin, and

$$\frac{d\sigma(\lambda, s_d)}{d\Omega_{\mathbf{k}}} = \int dM_{NN} \frac{d\sigma(\lambda, s_d)}{d\Omega_{\mathbf{k}} dM_{NN}}, \quad (17)$$

with

$$\frac{d\sigma(\lambda, s_d)}{d\Omega_{\mathbf{k}} dM_{NN}} = \sum_{s_1, s_2} \frac{(2\pi)^4}{4\omega} \frac{1}{2E_d(\mathbf{p}_d)} \int d\Omega_{\mathbf{p}_{NN}} \frac{p_{NN} k^2 m_N^2}{|kE - \mathbf{q} \cdot \hat{k} E_\pi(\mathbf{k})|} |M_{f,i}(E)|^2. \quad (18)$$

Here  $E = m_d + \omega$  is the total energy in the laboratory frame,  $\mathbf{p}_{NN}$  the momentum of  $N_1$  in the  $N_1 N_2$  CM frame, and  $M_{NN}$  the invariant mass of the two nucleons in the final  $\pi NN$  state. The magnitudes of the momenta are simply denoted, for example, by  $k \equiv |\mathbf{k}|$ , and  $\hat{k} \equiv \mathbf{k}/|\mathbf{k}|$ . To evaluate the Lorentz invariant amplitude  $M_{f,i}(E)$  using Eqs. (7)-(10), we need to express each outgoing momentum in Fig. 1 in terms of  $\mathbf{k}$ ,  $\hat{\mathbf{p}}_{NN}$  and  $M_{NN}$ . This can be done by using the standard Lorentz transformation. For a given  $\mathbf{k}$ ,  $M_{NN}$ , and the angles  $\Omega_{\mathbf{p}_{NN}}$ , we can calculate them by

$$p_{NN} = |\mathbf{p}_{NN}| = \sqrt{\frac{1}{4} M_{NN}^2 - m_N^2}, \quad (19)$$

$$\mathbf{p}_1 = \mathbf{p}_{NN} + \gamma \left( \frac{\gamma}{1 + \gamma} \boldsymbol{\beta} \cdot \mathbf{p}_{NN} - E_N(\mathbf{p}_{NN}) \right) \boldsymbol{\beta}, \quad (20)$$

$$\mathbf{p}_2 = \mathbf{P}_{NN} - \mathbf{p}_1, \quad (21)$$

with

$$\mathbf{P}_{NN} = \mathbf{q} - \mathbf{k}, \quad (22)$$

$$\boldsymbol{\beta} = -\frac{\mathbf{P}_{NN}}{[M_{NN}^2 + \mathbf{P}_{NN}^2]^{1/2}}, \quad (23)$$

$$\gamma = \frac{1}{\sqrt{1 - \boldsymbol{\beta}^2}}. \quad (24)$$

We will also present results of the differential cross section in the the CM frame of the  $\gamma$ - $d$  system. We find that

$$\frac{d\sigma}{d\Omega_c} \equiv \frac{d\sigma}{d\Omega_{\mathbf{k}_c}} = \frac{1}{6} \sum_{\lambda, s_d} \frac{d\sigma(\lambda, s_d)}{d\Omega_{\mathbf{k}_c}}, \quad (25)$$

where

$$\frac{d\sigma(\lambda, s_d)}{d\Omega_{\mathbf{k}_c}} = \int dM_{NN} \frac{d\sigma(\lambda, s_d)}{d\Omega_{\mathbf{k}_c} dM_{NN}}, \quad (26)$$

with

$$\frac{d\sigma(\lambda, s_d)}{d\Omega_{\mathbf{k}_c} dM_{NN}} = \sum_{s_1, s_2} \frac{1}{|\mathbf{v}_{\text{rel},c}|} \frac{(2\pi)^4}{4\omega_c} \frac{1}{2E_d(\mathbf{q}_c)} \int d\Omega_{\mathbf{P}_{NN}} \frac{p_{NN} k_c m_N^2}{E_c} |M_{f,i}(E_c)|^2, \quad (27)$$

where  $(\omega_c, \mathbf{q}_c)$  and  $E_c$  can be obtained from  $(\omega, \mathbf{q})$  and  $E$  in the laboratory frame by the Lorentz transformation with  $\boldsymbol{\beta} = \mathbf{q}/(\omega + m_d)$ . The momentum variables for the calculations of the invariant amplitudes using Eqs. (7)-(10) can be obtained from the same Eqs. (19)-(24), but setting  $\mathbf{P}_{NN} = -\mathbf{k}_c$ .

We will also present results for three polarization observables of current interest. We choose the  $z$ -axis along the incident photon direction,  $\mathbf{q} = (q_x, q_y, q_z) = (0, 0, q)$ , and the  $y$ -axis along the vector product,  $\hat{q} \times \hat{k}$ . Then, the photon asymmetry  $\Sigma$  for the  $d(\gamma, \pi)NN$  reaction is defined by

$$\Sigma_{\gamma d} = \frac{d\sigma(\lambda = 2) - d\sigma(\lambda = 1)}{d\sigma(\lambda = 2) + d\sigma(\lambda = 1)}, \quad (28)$$

where  $d\sigma(\lambda)$  denotes either of differential cross sections of Eqs. (16) or (25), but the initial photon polarization is fixed to  $\lambda$  instead of the average. The components  $\lambda = 1, 2$  for the linear photon polarization in Eq. (28) are

$$\boldsymbol{\epsilon}_{\lambda=1} = (1, 0, 0), \quad \boldsymbol{\epsilon}_{\lambda=2} = (0, 1, 0). \quad (29)$$

The asymmetry  $E$  of the circularly polarized photons on a deuteron target polarized along the  $z$ -axis ( $s_d = +1$ ) is defined by

$$E_{\gamma d} = \frac{d\sigma(\lambda = 3, s_d = +1) - d\sigma(\lambda = 4, s_d = +1)}{d\sigma(\lambda = 3, s_d = +1) + d\sigma(\lambda = 4, s_d = +1)}, \quad (30)$$

where  $d\sigma(\lambda, s_d = +1)$  denotes either of differential cross sections of Eqs. (17) or (26); the deuteron spin orientation is  $s_d = +1$  and the components  $\lambda = 3, 4$  for the circular photon polarization are defined as

$$\boldsymbol{\epsilon}_{\lambda=3} = \frac{+1}{\sqrt{2}}(1, -i, 0), \quad \boldsymbol{\epsilon}_{\lambda=4} = \frac{-1}{\sqrt{2}}(1, i, 0). \quad (31)$$

The asymmetry  $G$  of the linearly polarized photons on a polarized deuteron is defined by

$$G_{\gamma d} = \frac{d\sigma(\lambda = 5, s_d = +1) - d\sigma(\lambda = 6, s_d = +1)}{d\sigma(\lambda = 5, s_d = +1) + d\sigma(\lambda = 6, s_d = +1)}, \quad (32)$$

where the components  $\lambda = 5, 6$  for the photon polarization are

$$\boldsymbol{\epsilon}_{\lambda=5} = \frac{1}{\sqrt{2}}(1, 1, 0), \quad \boldsymbol{\epsilon}_{\lambda=6} = \frac{1}{\sqrt{2}}(1, -1, 0). \quad (33)$$

### III. RESULTS

In our calculations of the amplitudes Eqs. (8)-(10), the  $\gamma N, \pi N \rightarrow \pi N$  partial-wave amplitudes up to and including  $L = 5$  ( $L$ : the  $\pi N$  orbital angular momentum) generated from the ANL-Osaka model of Refs. [18, 19] are taken into account. To calculate the loop-integrations in Eqs. (9) and (10) for the  $N$ - and  $\pi$ -exchange mechanisms, respectively, the off-energy-shell two-body matrix elements are generated from solving the scattering equation Eq. (5) for the meson-nucleon scattering and a similar Lippmann-Schwinger equation of Eq. (A8) for the  $NN$  scattering. The  $NN \rightarrow NN$  partial wave amplitudes up to and including  $J = 3$  ( $J$ : the  $NN$  total angular momentum) generated from the CD-Bonn potential are included in the calculations.

We first compare our predictions with the available data of  $d(\gamma, \pi^0)pn$  and  $d(\gamma, \pi^-)pp$  reactions. We then examine whether our results can be improved if the employed  $\gamma N \rightarrow \pi N$  model of Ref. [19] is adjusted to also fit the recent Mainz data [25, 28] of  $\gamma n \rightarrow \pi^0 n$ . We also examine the roles of the off-energy-shell and FSI effects in explaining the data. The differences with the approach of Refs. [29, 30] will also be discussed.

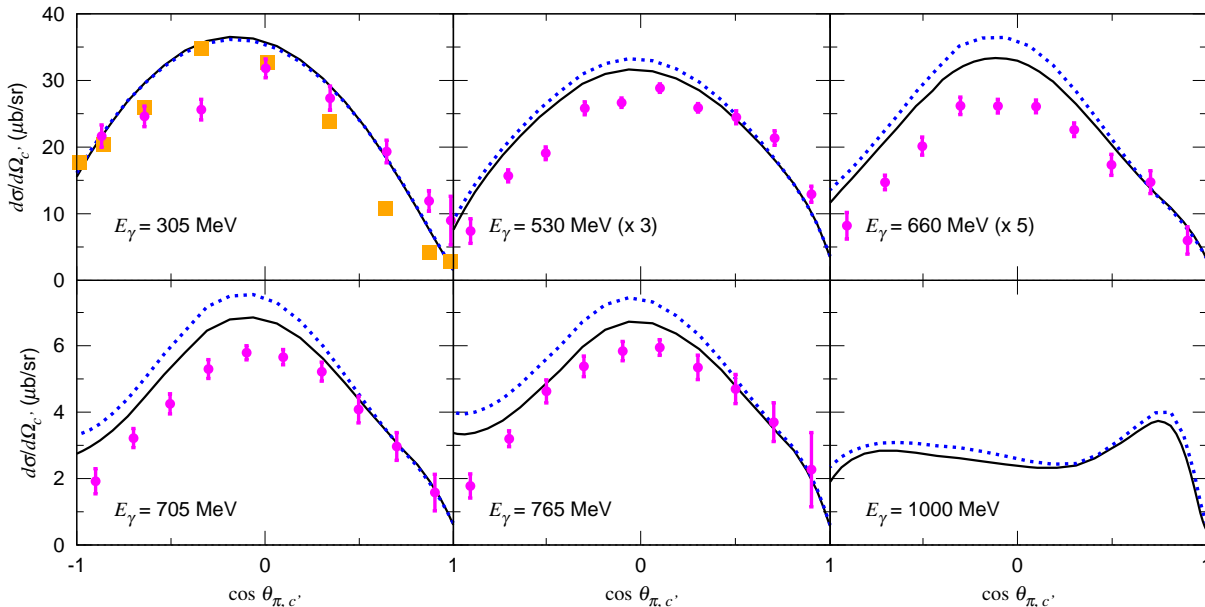


FIG. 2. Differential cross sections for  $d(\gamma, \pi^0)pn$  calculated with the  $\gamma N \rightarrow \pi N$  amplitudes from the AO model [18, 19] (blue dotted curves) and the new fits including the recent Mainz data [25, 28] of  $\gamma n \rightarrow \pi^0 n$  (black solid curves). The cross sections are scaled by the factor in the parenthesis when it is given. The pion emission angle  $\theta_{\pi, c'}$  is defined in the frame where the photon momentum  $\mathbf{q}_{c'}$  and the deuteron momentum  $\mathbf{p}_{d, c'}$  are related by  $\mathbf{p}_{d, c'} = -2\mathbf{q}_{c'}$ . The photon energies indicated in the panels ( $E_\gamma$ ) are those in the laboratory frame. Data are from Ref. [48] (magenta circles) and Ref. [49] (orange squares).

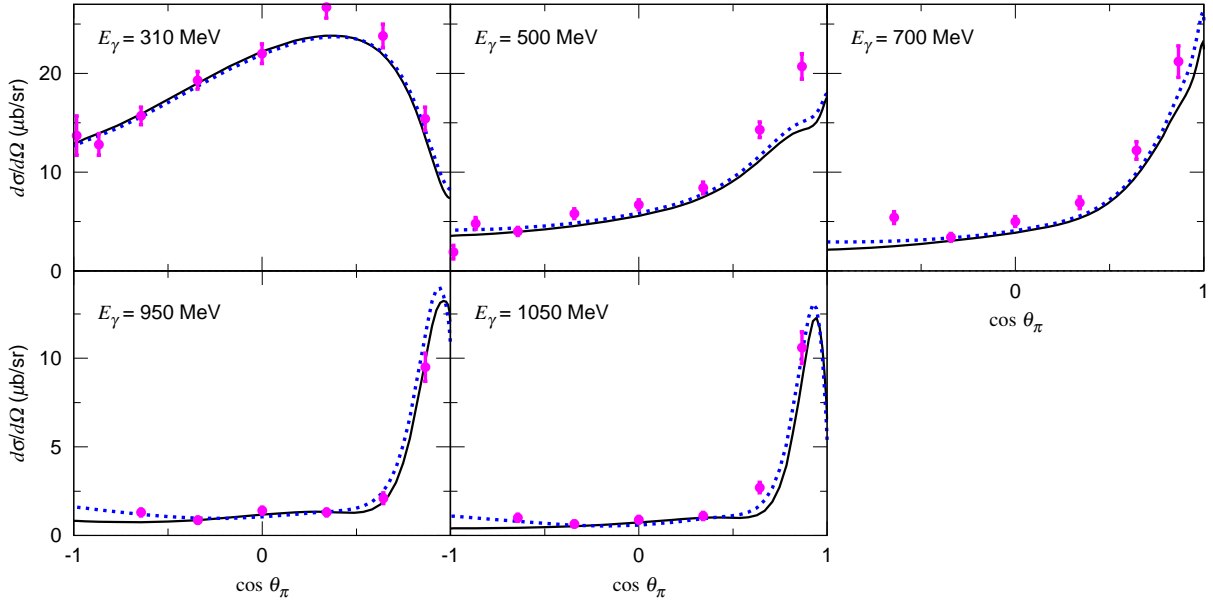


FIG. 3. Differential cross sections for  $d(\gamma, \pi^-)pp$  in the laboratory frame. Data are from Ref. [50]. The other features are the same as those in Fig. 2.

#### A. Comparisons with data of $d(\gamma, \pi)NN$ reactions

We have found that our predictions agree reasonably well with the available data of  $d(\gamma, \pi^0)pn$  and  $d(\gamma, \pi^-)pp$  reactions. In Figs. 2 and 3, we show some typical comparisons of the data for unpolarized differential cross sections and our results (blue dotted curves) using the amplitudes generated from the ANL-Osaka model. Clearly there are some discrepancies with the data, in particular for  $d(\gamma, \pi^0)np$  in the  $E_\gamma = 500\text{--}750$  MeV region ( $E_\gamma$  is the photon energy in the laboratory frame). One possible source of the discrepancies is that, when determining the parameters for the ANL-Osaka model, we used rather scarce  $\gamma n \rightarrow \pi^0 n$  dataset that are extracted from  $d(\gamma, \pi^0)np$  data. To see whether this is the case, we have extended the fit of Ref. [19] to also include recently extracted data for  $\gamma n \rightarrow \pi^0 n$  from Mainz [25, 28], and also recent data for  $\gamma n \rightarrow \pi^- p$  from JLab [22, 23]. However, the amount of these new data are much less than the total number of the world data for  $\pi N, \gamma N \rightarrow \pi N, \eta N, K\Lambda, K\Sigma$  included in the fit [18, 19] for the ANL-Osaka model. We thus do not expect that the resonance parameters and the hadronic parameters determined in Ref. [19] will be changed significantly by including the recent  $\gamma n \rightarrow \pi N$  data, and therefore vary only the parameters for the bare  $\gamma n \rightarrow N^*$  couplings in the new fit.

To be consistent with the procedure in constructing the ANL-Osaka model, the calculations for the fits include  $L = 0 - 10$  partial waves. In addition to the data of  $\pi p, \gamma p \rightarrow \pi N, \eta N, K\Lambda, K\Sigma$  and  $\gamma n \rightarrow \pi^0 n, \pi^- p$  included in the fits in Ref. [19], the recent data [22, 23, 25, 28] of the unpolarized differential cross sections and  $E$  for  $\gamma n \rightarrow \pi^0 n, \pi^- p$  are included in the new fits. In Fig. 4, we show the comparisons of our results with the data of the differential cross sections. The fits to the data which are not shown in Fig. 4 are of similar quality and hence are omitted to simplify the presentation. Clearly, the results from this new fit (red solid curves) and those from the ANL-Osaka model (blue dashed curves) are

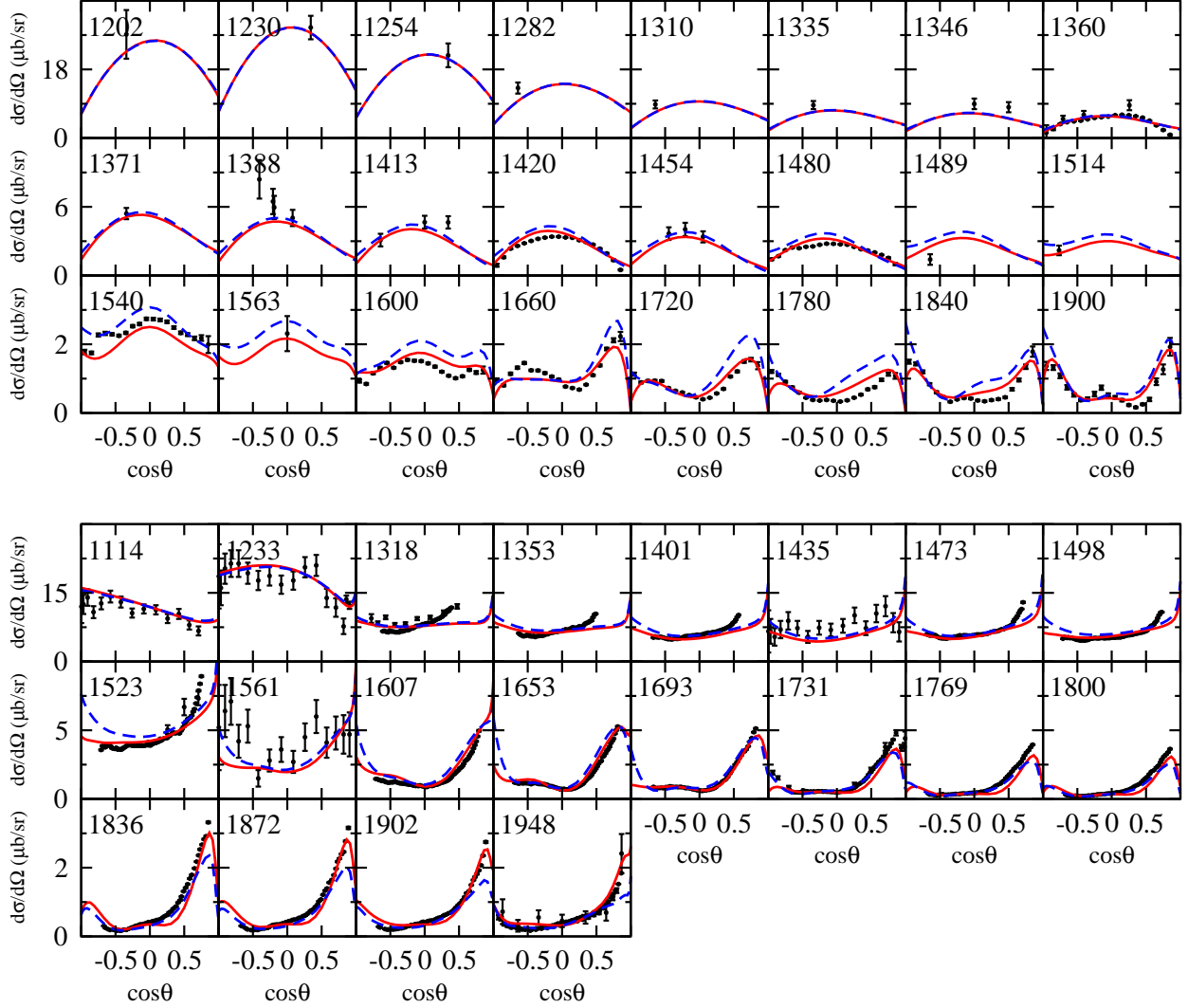


FIG. 4. Differential cross sections for  $\gamma n \rightarrow \pi^0 n$  (upper panel) and for  $\gamma n \rightarrow \pi^- p$  (lower panel) in the CM frame. The number in each of the panels is the total energy in unit of MeV. The red solid curves are from the new fit while the blue dashed curves are from the AO model [19]. The data are from Ref. [25] for  $\gamma n \rightarrow \pi^0 n$  and Ref. [23] for  $\gamma n \rightarrow \pi^- p$  in addition to those from the database of the INS DAC Services [51].

very similar. On the other hand, we see in Fig. 5 some large differences between the fits and the data for the polarization observable  $E$ . Further improvements are possible only if we also vary the non-resonant parameters around the values determined in Ref. [19]. This will be worthwhile to pursue when the data for other spin observables, such as  $G$  and  $\Sigma$ , become available. For our present purposes, the quality of the fit shown in Figs. 4-5 is sufficiently good. We note here that the higher partial waves ( $L = 6 - 10$ ), which include only non-resonant Born amplitudes, just slightly change the shape of the angular distributions for  $\gamma n \rightarrow \pi^- p$  in the forward pion kinematics, and has little effects on  $\gamma n \rightarrow \pi^0 n$ . These weak higher partial wave amplitudes are therefore neglected in all of our calculations for the  $d(\gamma, \pi)NN$  reactions.

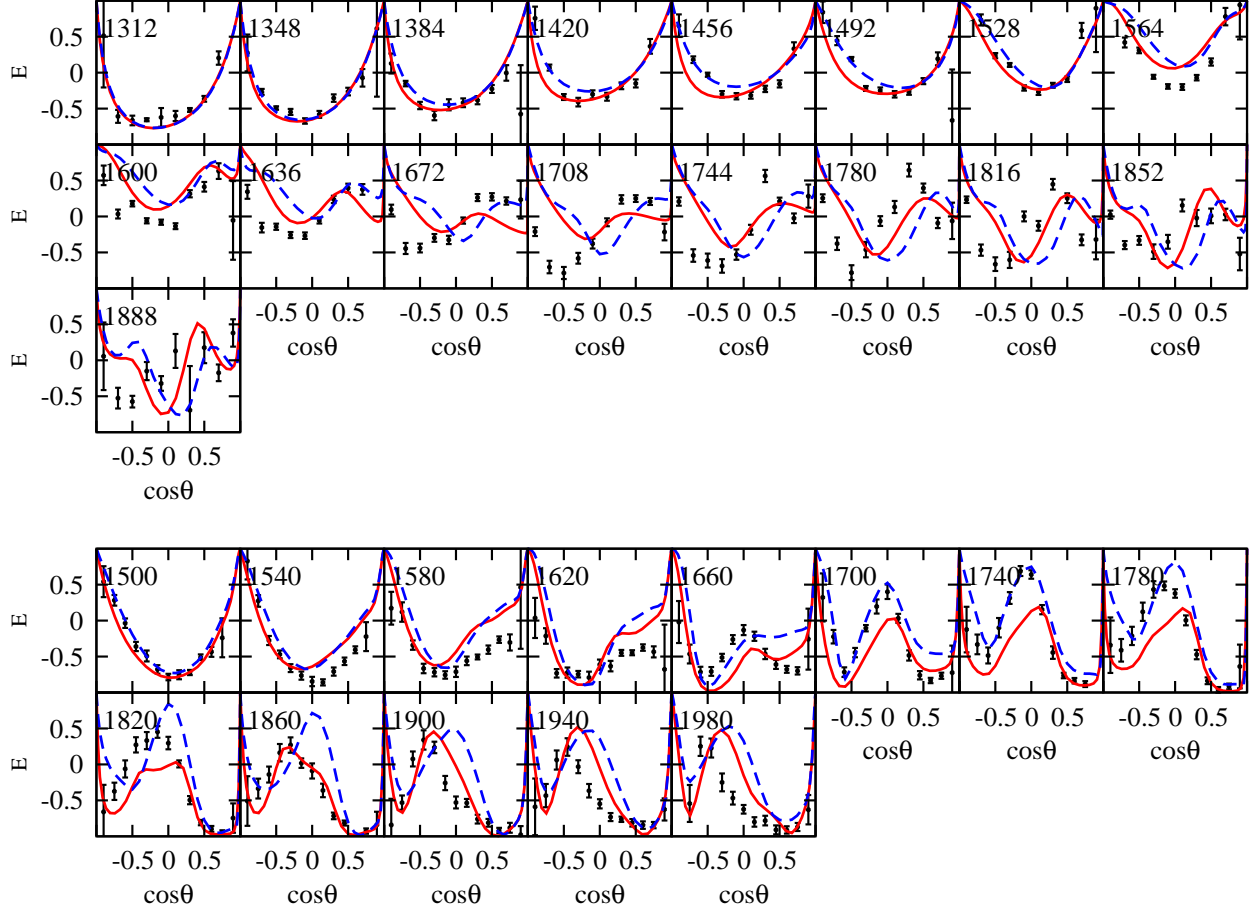


FIG. 5. The polarization observable  $E$  for  $\gamma n \rightarrow \pi^0 n$  (upper panel) and  $\gamma n \rightarrow \pi^- p$  (lower panel). The data are from Ref. [28] for  $\gamma n \rightarrow \pi^0 n$  and Ref. [22] for  $\gamma n \rightarrow \pi^- p$ . The other features are the same as those in Fig. 4.

With the parameters from the new fits, the calculated differential cross sections for  $d(\gamma, \pi^0)pn$  and  $d(\gamma, \pi^-)pp$  are the solid curves in Figs. 2 and 3. Comparing with the blue dotted curves from using the ANL-Osaka amplitudes, we see that the agreements with the data for  $d(\gamma, \pi^0)pn$  in the region  $E_\gamma = 500 - 700$  MeV are improved, but some significant discrepancies with the data remain. It could be due to the neglect of higher order terms in our multiple scattering calculations such as  $\rho$ -,  $\sigma$ -, and  $\Delta$ -exchange terms. On the other hand, we must examine critically the procedures used in extracting the  $\gamma n \rightarrow \pi^0 n, \pi^- p$  cross sections from the data of  $d(\gamma, \pi)NN$ . This is the subject we will address in Sec. IV. The results presented in the rest of this paper are from using the parameters from the new fit.

## B. Off-shell effects

In Sec. II, we show that the two-body matrix elements in the calculations of  $d(\gamma, \pi)NN$  amplitudes can be off-energy-shell within the Hamiltonian formulation where all particles are on their mass-shell. In Fig. 6, we see that, if we set all two-body matrix elements in Eqs. (8)–(10) to their on-shell values, the full results (solid curves) are changed to the blue

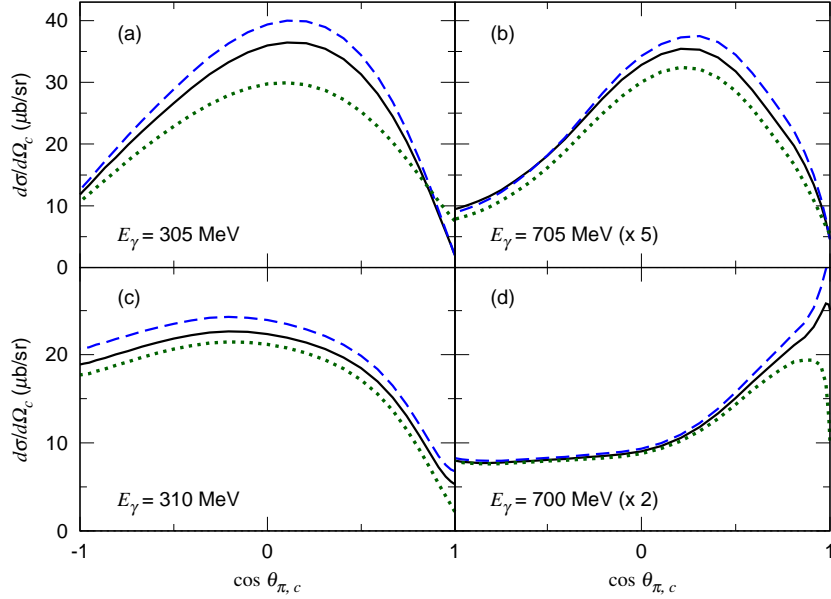


FIG. 6. The off-shell effects on differential cross sections for  $d(\gamma, \pi^0)pn$  (a,b) and  $d(\gamma, \pi^-)pp$  (c,d) in the CM frame. The photon energy and the scaling factor are indicated in each figure. Solid curves: full calculations; dashed curves: the  $\gamma N \rightarrow \pi N$ ,  $NN \rightarrow NN$ , and  $\pi N \rightarrow \pi N$  amplitudes are put on-shell; dotted curves: only pole terms are kept in loop integrations [see Eq. (34)].

dashed curves. In general, the effects are more significant at low energies and less at higher energies, as illustrated at energies near 300 and 700 MeV in Fig. 6. The differences between the solid and blue dashed curves suggest that the  $\gamma n \rightarrow \pi^- p$  extracted using the on-shell calculation results of Refs. [29] are reasonable, but could be modified if the off-shell effects are included in their formulation. The off-shell effects are however model dependent and one must use well-established physics to determine them. In our approach, the off-shell effects are determined by the meson-exchange mechanisms in the ANL-Osaka model and CD-Bonn  $NN$  potential. Similar considerations must also be taken in other approaches.

If we further keep only the on-shell pole terms of the propagators by setting

$$\frac{1}{E - E_N(\mathbf{p}_1) - E_N(\mathbf{p}_2) - E_\pi(\mathbf{k}) + i\epsilon} \rightarrow -i\pi\delta(E - E_N(\mathbf{p}_1) - E_N(\mathbf{p}_2) - E_\pi(\mathbf{k})) , \quad (34)$$

in the loop integrations in Eqs. (9) and (10), we obtain the green dotted curves. Clearly, they are significantly different from the solid curves of the full calculations including the off-shell effects, in particular, at  $E_\gamma = 305$  MeV for  $d(\gamma, \pi^0)pn$ , and in the forward angles ( $\cos \theta_{\pi,c} \rightarrow 1$ ) at  $E_\gamma = 700$  MeV for  $d(\gamma, \pi^-)pp$ . Here we mention that Eq. (34) is sometimes used to reduce the computation effort for the loop-integration. The differences between the solid and dotted curves in Fig. 6 give some estimates on the accuracy of such a simplified approach which neglects the off-shell effects completely.

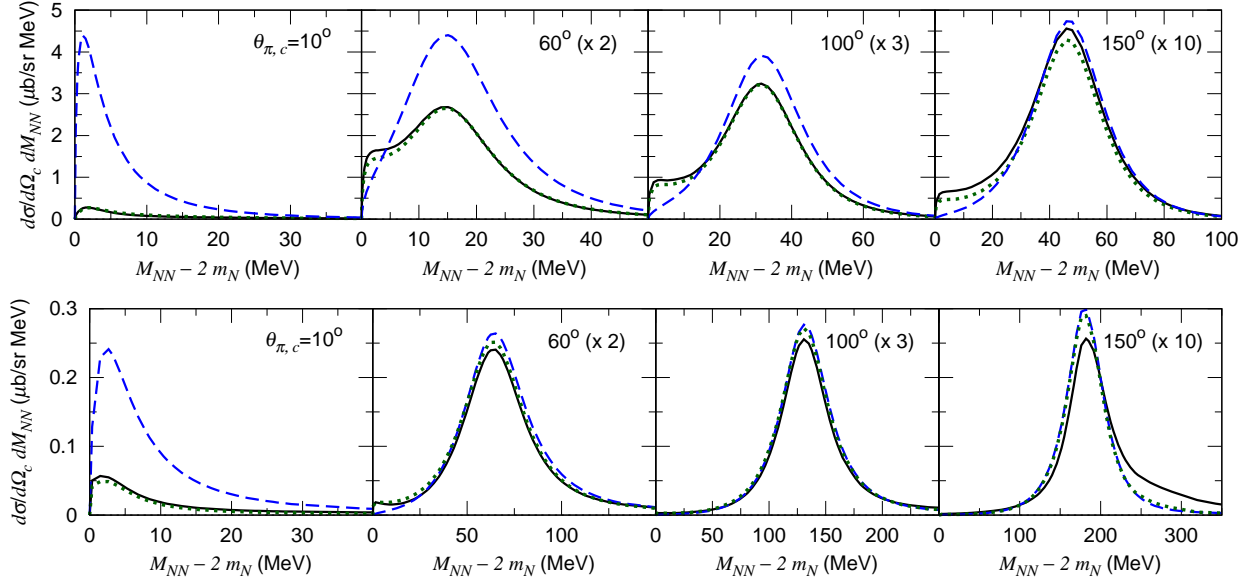


FIG. 7. The  $NN$  invariant mass distribution for  $d(\gamma, \pi^0)pn$  at  $E_\gamma = 305$  MeV (upper row) and  $E_\gamma = 705$  MeV (lower row). The pion emission angle in the CM frame along with the scaling factor is indicated in each figure. Dashed curves: impulse; dotted curves: impulse +  $N$ -exchange; solid curves: impulse +  $N$ -exchange +  $\pi$ -exchange.

### C. Final state interaction effects

In all of the previous investigations of  $d(\gamma, \pi^0)pn$  reaction, the  $N$ -exchange term illustrated in Fig. 1(b) is found to dominant the FSI. This can be examined by using Eq. (27) to calculate the dependence of the differential cross sections on the  $NN$  invariant mass  $M_{NN}$ . In the upper half of Fig. 7, we see at a small angle of  $10^\circ$  that the main contributions to the differential cross sections of  $d(\gamma, \pi^0)pn$  at  $E_\gamma = 305$  MeV are in the region close to the  $NN$  threshold ( $M_{NN} - 2m_N \sim 0$ ) where the  $NN$  scattering is dominated by the  ${}^3S_1 + {}^3D_1$  partial wave which is orthogonal to the deuteron bound state. Consequently, the  $NN$  FSI greatly reduces the cross section of the impulse ( $t^{\text{imp}}$ ) term (dashed curve) to that of the  $t^{\text{imp}} + t^{N\text{-exc}}$  terms (dotted curve). When the pion-exchange term ( $t^{\pi\text{-exc}}$ ) is included, we obtain the solid curve which is almost indistinguishable from the dotted curve. As the scattering angle increases to  $60^\circ$ , the peak position of the  $M_{NN}$  spectrum is shifted to the larger invariant mass region where the reduction due to the  $NN$  FSI is still large, but much less than that in the forward angles. The FSI effects become weak at large angles  $100^\circ$  and  $150^\circ$  since the large portion of the  $NN$  spectrum is in the region far away from the  $NN$  threshold.

At a higher photon energy of  $E_\gamma = 705$  MeV (lower half of Fig. 7), the reduction due to the  $NN$  FSI is similarly dependent on how close the  $M_{NN}$  spectrum peak is to the  $NN$  threshold. We also note that while the  $\pi N$  FSI effect is much smaller than the  $NN$  FSI effect overall, it can give a main FSI correction at large pion emission angles; for example, see the results at  $\theta_{\pi,c} \sim 150^\circ$  in the lower half of Fig. 7. Integrating over  $M_{NN}$ , the FSI effects on the differential cross sections of  $d(\gamma, \pi^0)pn$  are shown in Fig. 8. The large reduction due to the  $NN$  FSI is clear. Clearly, the large reduction due to FSI is essential in obtaining

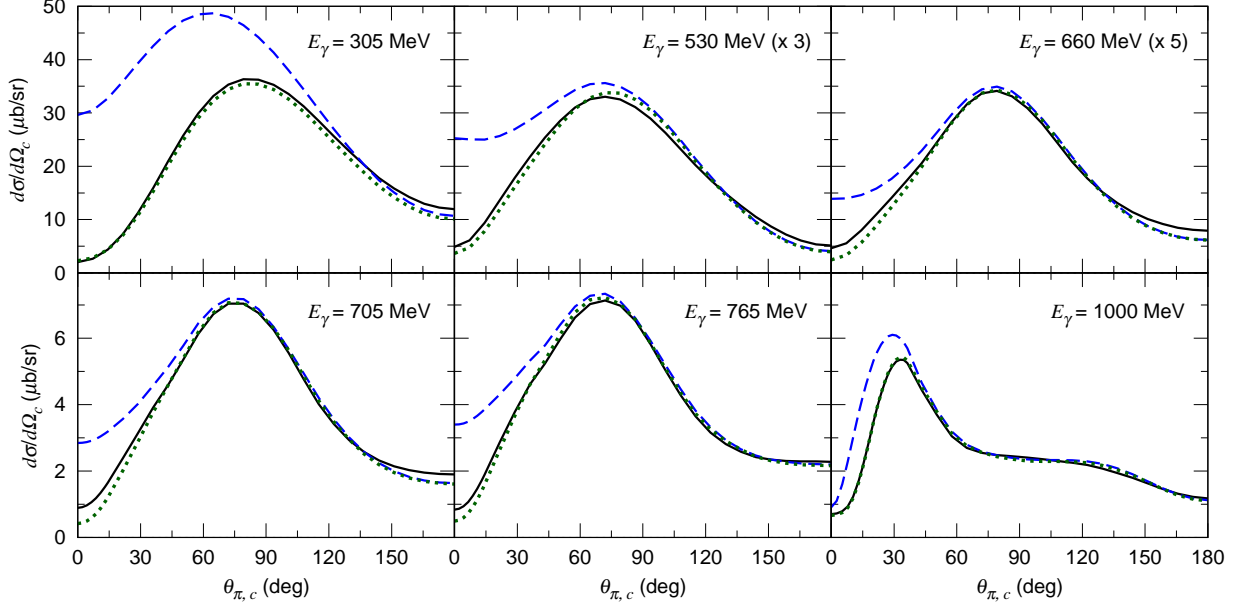


FIG. 8. Differential cross sections for  $d(\gamma, \pi^0)pn$  in the CM frame. The reaction mechanisms included in the calculations for each of the curves are the same as those in Fig. 7.

a reasonable agreement with the data in Fig. 2. (Note that the results in Fig. 2 is given in a different frame chosen in Ref. [48] to present the data). This is similar to the previous findings [30, 33, 34]. The FSI effects at higher energies are weaker, but still significant in the forward angle,  $\theta_{\pi,c} \sim 0^\circ$ .

The FSI effects on  $d(\gamma, \pi^-)pp$  are shown in Fig. 9. Here, we see that the FSI effect is also clearly visible in the small angle region where the  $M_{NN}$  spectrum peak is close to the  $NN$  threshold and hence the  $NN$  FSI going to the  $^1S_0$   $NN$  partial wave gives a dominant portion of the FSI effect. Contrary to the  $d(\gamma, \pi^0)pn$  case, its interference with the impulse term is to enhance the cross section from the dashed curves to the dotted curves. The  $\pi N$  FSI effect is also weak here, as can be seen in the negligible difference between the solid and dotted curves. As the angle increases, the  $\pi N$  FSI effect is getting discernible but overall the FSI effect quickly becomes much smaller. Therefore, the FSI effect on the differential cross sections are very weak, as seen in Fig. 10.

We have also investigated the FSI effects on the polarization observables  $\Sigma$ ,  $E$ , and  $G$  defined in Eqs. (28)-(32) which are of current interests. The results are shown in Figs. 11 and 12. Clearly, the FSI effects do not play an important role here. It will be interesting to compare our predictions with the data in near future.

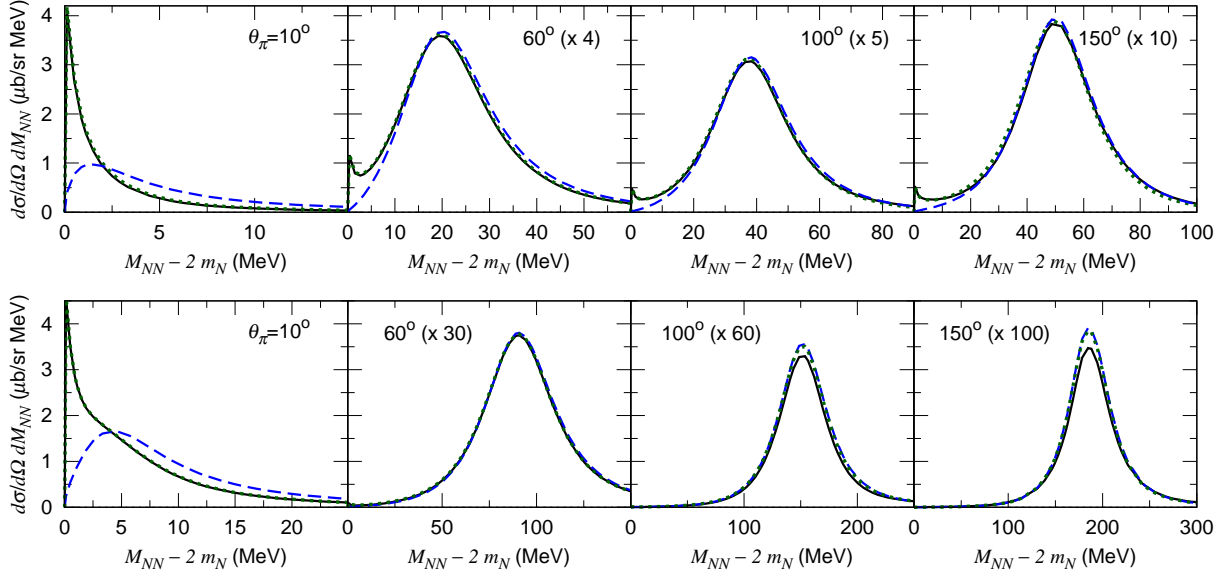


FIG. 9. The  $NN$  invariant mass distribution for  $d(\gamma, \pi^-)pp$  at  $E_\gamma = 310$  MeV (upper row) and  $E_\gamma = 700$  MeV (lower row). The pion emission angles indicated in the figures are those in the laboratory frame. The reaction mechanisms included in the calculations for each of the curves are the same as those in Fig. 7.

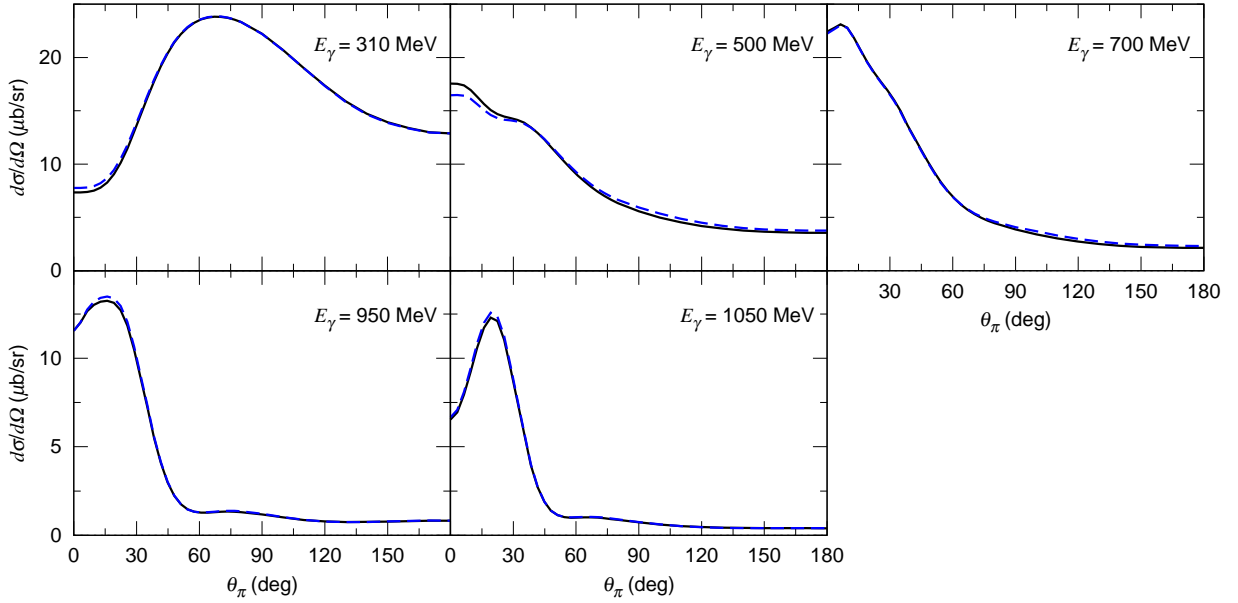


FIG. 10. Differential cross sections for  $d(\gamma, \pi^-)pp$  in the laboratory frame. The reaction mechanisms included in the calculations for each of the curves are the same as those in Fig. 7.

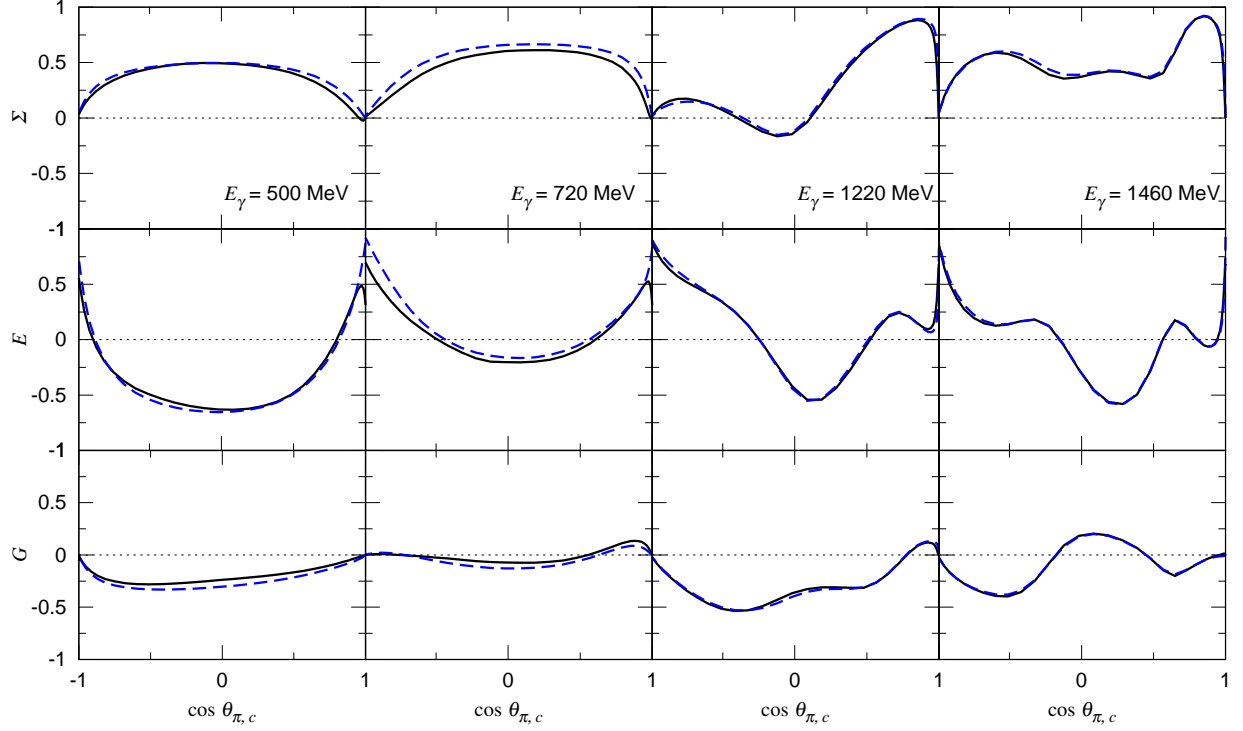


FIG. 11. The polarization observables  $\Sigma$ ,  $E$ , and  $G$  for  $d(\gamma, \pi^0)pn$  in the CM frame. Dashed curves: impulse; solid curves: impulse +  $N$ -exchange +  $\pi$ -exchange.

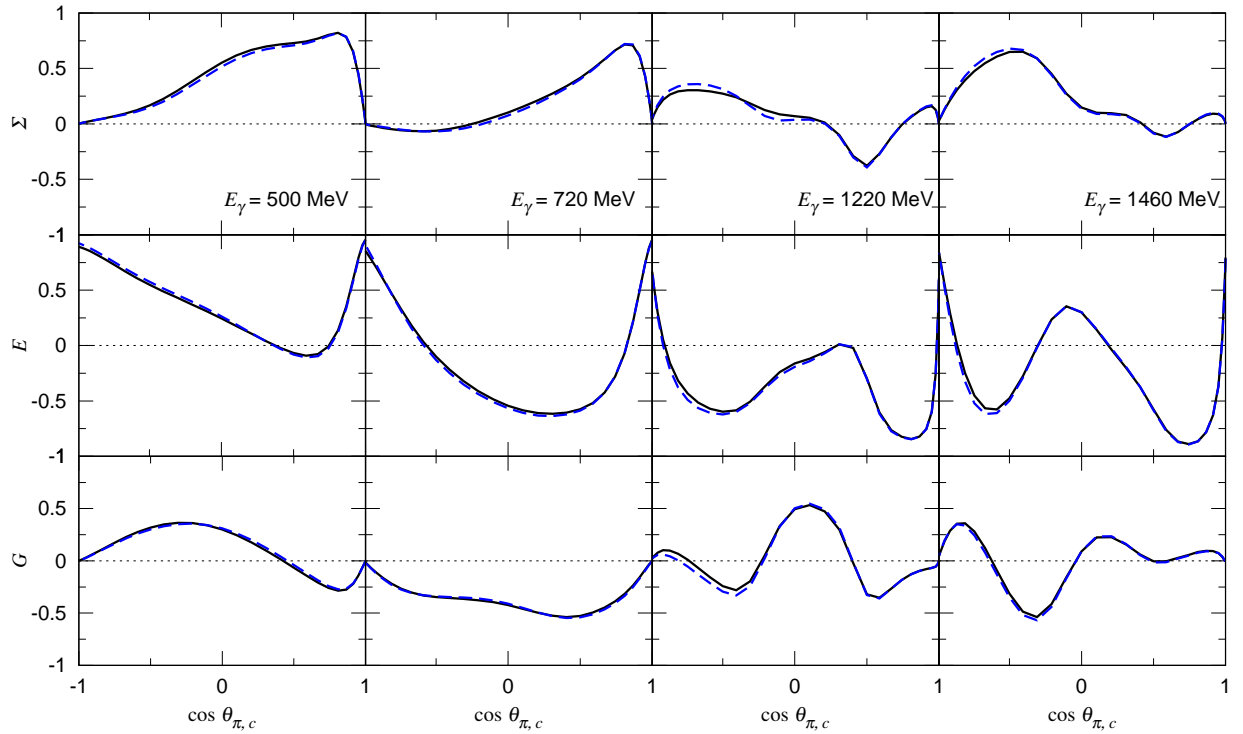


FIG. 12. The polarization observables  $\Sigma$ ,  $E$ , and  $G$  for  $d(\gamma, \pi^-)pp$  in the CM frame. The other features are the same as those in Fig. 11.

#### IV. EXTRACTION OF $\gamma n \rightarrow \pi N$ CROSS SECTIONS FROM $d(\gamma, \pi)NN$ DATA

We now turn to investigating the extractions of the unpolarized cross sections and polarization observables for the  $\gamma N \rightarrow \pi N$  from the data of  $d(\gamma, \pi)NN$  reactions.

##### A. Unpolarized cross sections

For extracting cross sections of  $\gamma N \rightarrow \pi N$  from those of  $d(\gamma, \pi)NN$ , we need a formula that gives a relation between them. For deriving it, we first consider an ideal situation that the incident photon interacts with only one of the nucleons inside the deuteron [Fig. 1(a)]. The cross section for this ‘quasi-free’ process can be calculated from keeping only the first term  $t_{f,i}^{\text{imp}}$  of Eq. (7) in our calculations; the FSI terms and exchange terms are neglected. In this simplified situation, it is straightforward to derive from Eq. (15) that the  $d(\gamma, \pi)N_1N_2$  cross section ( $\sigma_{\gamma d}$ ) is related to the  $\gamma N \rightarrow \pi N_1$  cross section ( $\sigma_{\gamma N}$ ) by

$$\frac{d^2\sigma_{\gamma d}(E_\gamma)}{dW d\cos\theta} = \phi(W; E_\gamma) \frac{E'_\gamma}{E_\gamma} \frac{d\sigma_{\gamma N}(W)}{d\cos\theta}, \quad (35)$$

where  $E_\gamma$  is the photon energy in the  $\gamma$ - $d$  laboratory frame,  $W$  is the invariant mass of the final  $\pi N_1$  system, and  $\theta$  the angle between the momenta of  $\gamma$  and  $\pi$  in the  $\pi N_1$  CM frame. The quantity  $E'_\gamma$  is defined by  $E'_\gamma = (W^2 - m_N^2)/(2m_N)$  and thus is the photon energy in the laboratory frame for  $\gamma N \rightarrow \pi N_1$ . The function  $\phi(W; E_\gamma)$  describes the probability of finding a process where the incident photon having  $E_\gamma$  hits a nucleon in the deuteron with an invariant mass  $W$ , and is determined by the nucleon momentum distribution  $\rho_d(|\mathbf{p}_s|)$ , as defined in Eq. (A10), in the deuteron:

$$\phi(W; E_\gamma) = \int d^3p_s \frac{m_N}{E_N(\mathbf{p}_s)} \delta(W - w(\mathbf{p}_s, E_\gamma)) \frac{\rho_d(|\mathbf{p}_s|)}{4\pi}, \quad (36)$$

with

$$w(\mathbf{p}_s, E_\gamma) = \sqrt{(E_\gamma + m_d - E_N(\mathbf{p}_s))^2 - (\mathbf{q}_\gamma - \mathbf{p}_s)^2}, \quad (37)$$

where  $\mathbf{q}_\gamma$  ( $\mathbf{p}_s$ ) is the momentum of the incident photon (the spectator nucleon) in the  $\gamma$ - $d$  laboratory frame. Strictly speaking, Eq. (35) holds exactly only when ignoring the small deuteron  $d$ -state, although we do not make this additional simplification in our numerical analysis below of extracting cross sections of  $\gamma n \rightarrow \pi N$  from those of  $d(\gamma, \pi)NN$  with the use of Eq. (35) and its extension Eq. (38). Equations (35)-(36) agree with the formula used in Ref. [29] and the previous investigations [52–54]. Note that our definition for  $E'_\gamma$  is somewhat different from the one used in Refs. [29, 30].

In contrast to the above ideal situation, the photon in reality can hit the other nucleon and FSI can also occur. To isolate the cross sections associated with the quasi-free process, the conventional procedure is to apply a set of kinematical cuts to select the data. Within our model, this amounts to imposing the cuts when performing the phase-space integral in Eq. (15) to obtain a modified  $d(\gamma, \pi)NN$  cross section,  $\left. \frac{d^2\sigma_{\gamma d}(E_\gamma)}{dW d\cos\theta} \right|_{\text{cut}}$ , and *assume* that this quantity is solely from the quasi-free mechanism integrated over the same phase-space. The resulting formula that can be used in analyzing data is

$$\left. \frac{d^2\sigma_{\gamma d}(E_\gamma)}{dW d\cos\theta} \right|_{\text{cut}} = \phi_{\text{cut}}(W; E_\gamma) \frac{E'_\gamma}{E_\gamma} \frac{d\sigma_{\gamma N}(W)}{d\cos\theta}, \quad (38)$$

TABLE I. Three sets of kinematical cuts (Cut A, B, and C). The cuts in 4-7th rows have been used in the references listed in the second row when extracting  $\gamma n \rightarrow \pi^- p$  observables (specified in the parentheses) from  $d(\gamma, \pi^-)pp$  data for the range of the photon energies listed in the third row. The azimuthal angle difference between  $\pi^-$  and the faster proton is denoted by  $\Delta\phi$ .

Ref.	Cut A	Cut B	Cut C
$E_\gamma$ (MeV)	[20] ( $d\sigma/d\Omega$ )	[23] ( $d\sigma/d\Omega$ )	[22] ( $E$ )
	301 - 455	445 - 2510	700 - 2400
$\pi^-$ momentum (MeV)	> 80	> 100	> 400
Faster proton momentum (MeV)	> 270	> 360	> 400
Slower proton momentum (MeV)	< 270	< 200	< 100
$\Delta\phi =  \phi_{\pi^-} - \phi_{\text{faster proton}} $	-	-	$160^\circ < \Delta\phi < 200^\circ$

with

$$\phi_{\text{cut}}(W; E_\gamma) = \int d^3p_s \frac{m_N}{E_N(\mathbf{p}_s)} \delta(W - w(\mathbf{p}_s, E_\gamma)) \frac{\rho_d(|\mathbf{p}_s|)}{4\pi} \prod_i \theta(x_i^{\text{max}} - x_i) \theta(x_i - x_i^{\text{min}}) \quad (39)$$

where  $\{x_i\}$  are a set of kinematical variables and  $x_i^{\text{min}}$  ( $x_i^{\text{max}}$ ) is the minimum (maximum) value allowed by the cut. Also, we need to make clear the meanings of  $W$  and  $\theta$  in Eq. (38). When the cross sections of  $\gamma n \rightarrow \pi^0 n$  are extracted from those of  $d(\gamma, \pi^0)pn$ ,  $W$  is the final  $\pi^0 n$  invariant mass, and  $\theta$  the angle between the momenta of  $\gamma$  and  $\pi^0$  in the final  $\pi^0 n$  CM frame. When the cross sections of  $\gamma n \rightarrow \pi^- p$  are extracted from those of  $d(\gamma, \pi^-)pp$ , on the other hand, we identify one of the final protons having a larger momentum with the struck proton ( $p_{\text{struck}}$ ) and take  $W$  as the final  $\pi^- p_{\text{struck}}$  invariant mass and  $\theta$  the angle between  $\gamma$  and  $\pi^-$  momenta in the final  $\pi^- p_{\text{struck}}$  CM frame.

To proceed, we need to specify the kinematical cuts used in our investigations. Here we consider those employed in recent experimental analyses [20, 22, 23] to extract  $\gamma n \rightarrow \pi^- p$  observables from the  $d(\gamma, \pi^-)pp$  data, as summarized in Table I. For investigating the extraction of  $\gamma n \rightarrow \pi^0 n$  observable, we apply the same cuts to  $d(\gamma, \pi^0)pn$  by making obvious changes in the first column of Table I; ' $\pi^-$ '  $\rightarrow$  ' $\pi^0$ ', 'Faster proton'  $\rightarrow$  'Neutron', and 'Slower proton'  $\rightarrow$  'Proton'. When extracting the  $\gamma n \rightarrow \pi N$  observables in this paper, we use Cut A (Cut B) for  $E_\gamma = 300$  (500) MeV. For  $E_\gamma > 700$  MeV, Cut B (Cut C) is used for investigating the extractions of unpolarized differential cross sections (the polarization asymmetries  $\Sigma$ ,  $E$ , and  $G$ ). We always take the above choices for the cuts, unless otherwise stated.

To implement any one of the kinematical cuts listed in Table I into the numerical computations, it is most convenient to use the Monte-Carlo method to calculate the phase-space integrals for the  $d(\gamma, \pi)NN$  cross sections [Eqs. (16)-(18)] and  $\phi_{\text{cut}}(W; E_\gamma)$  of Eq. (39). The bin sizes (resolutions) for  $\cos\theta$  and  $W$  are taken to be 0.1 and 10 MeV, respectively, and thus a numerical value at  $x$  ( $= \cos\theta, W$ ) is understood to be the average over the range of  $x - \Delta/2 \leq x \leq x + \Delta/2$  where  $\Delta$  is the bin size. Therefore, all the numerical results (except those for free  $\gamma N \rightarrow \pi N$  observables) in this section are given with central values and their statistical errors associated with the Monte-Carlo method.

Our investigation is as follows. For a given choice of the kinematical cuts, we generate  $\left. \frac{d^2\sigma_{\gamma d}(E_\gamma)}{dW d\cos\theta} \right|_{\text{cut}}$  from our model as the 'data' for extracting the  $\frac{d\sigma_{\gamma N}(W)}{d\cos\theta}$  of  $\gamma N \rightarrow \pi N$  by using

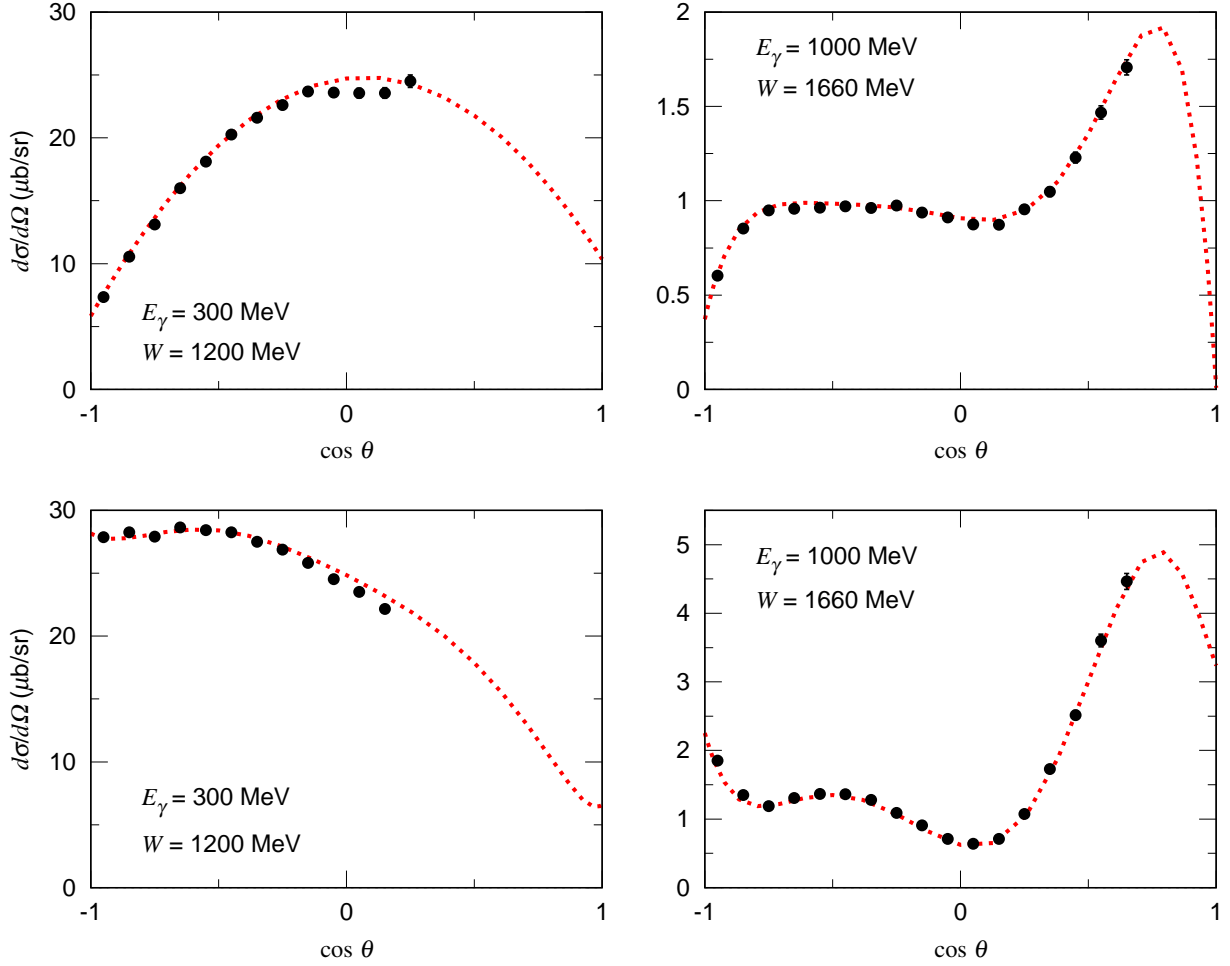


FIG. 13. Upper (Lower) panels: differential cross sections for  $\gamma n \rightarrow \pi^0 n$  ( $\gamma n \rightarrow \pi^- p$ ) in the CM frame. The black circle points with error bars in the upper (lower) panels are extracted using Eq. (38) from  $d(\gamma, \pi^0)pn$  ( $d(\gamma, \pi^-)pp$ ) differential cross sections generated from our model including only the quasi-free process. The errors are only statistical from the Monte-Carlo integral, and are not shown when smaller than the point size. The kinematical cuts used in calculating the  $d(\gamma, \pi)NN$  cross sections are explained in the text. The photon energy ( $E_\gamma$ ) in the laboratory frame and the final  $\pi N$  invariant mass ( $W$ ) for  $d(\gamma, \pi)NN_s$  ( $N_s$ : spectator nucleon) are indicated in the figure. The red dotted curves are the free  $\gamma n \rightarrow \pi N$  cross sections from the AO model for the total energy  $W$ .

Eq. (38). By comparing the extracted  $\frac{d\sigma_{\gamma N}(W)}{d\cos\theta}$  with the corresponding one on a free neutron, which are calculated with the same elementary amplitudes used in calculating  $\left.\frac{d^2\sigma_{\gamma d}(E_\gamma)}{dWd\cos\theta}\right|_{\text{cut}}$ , we can examine the extent to which the extracted cross sections could be distorted by the FSI and/or the kinematical cuts.

For each choice of the kinematical cuts, we use our model to generate three sets of ‘data’,  $\left.\frac{d^2\sigma_{\gamma d}(E_\gamma)}{dWd\cos\theta}\right|_{\text{cut}}$ , from (1) quasi-free process as defined above Eq. (35), (2) impulse +  $N$ -exchange, and (3) impulse +  $N$ -exchange +  $\pi$ -exchange. The  $\gamma N \rightarrow \pi N$  differential cross section  $d\sigma_{\gamma N}(W)/d\cos\theta$  can then be extracted from each dataset by using Eq. (38). In all of

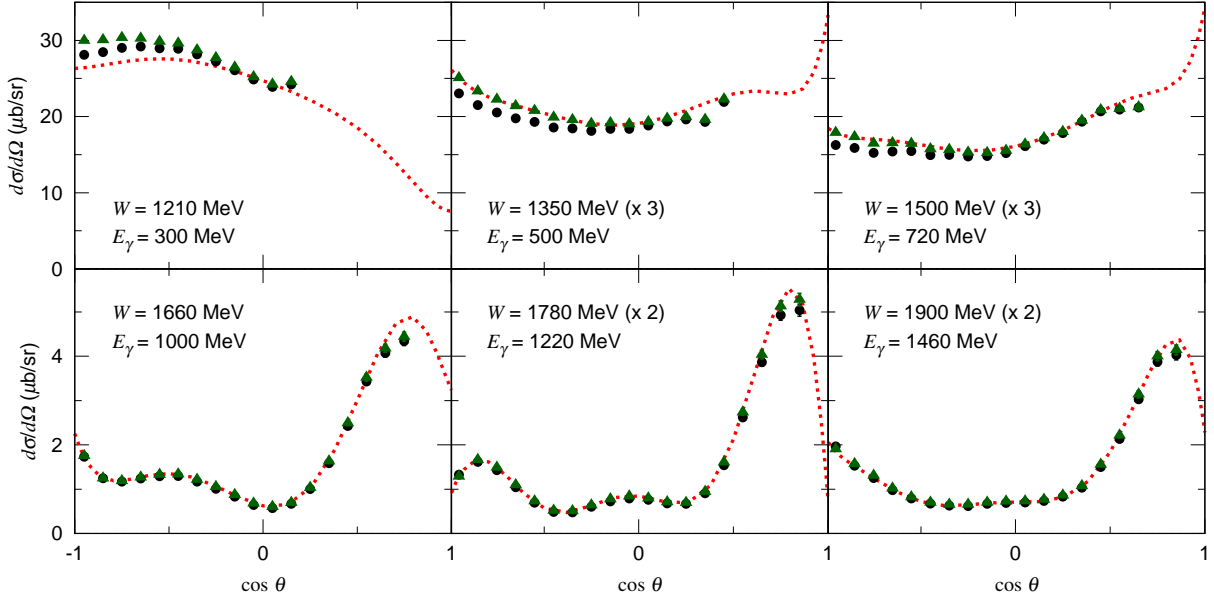


FIG. 14. The pion angular distribution in the CM frame for  $\gamma n \rightarrow \pi^- p$ . The black circles (green triangles) with error bars are extracted using Eq. (38) from  $d(\gamma, \pi^-)pp$  differential cross sections generated by our model including the impulse +  $N$ -exchange +  $\pi$ -exchange (impulse +  $N$ -exchange) terms. The kinematical cuts used in calculating the  $d(\gamma, \pi^-)pp$  cross sections are explained in the text. The photon energy ( $E_\gamma$ ) in the laboratory frame and the final  $\pi^- p$  invariant mass ( $W$ ) for  $d(\gamma, \pi^-)pp$  are indicated in the figure. The errors are only statistical from the Monte-Carlo integral, and are not shown when smaller than the point size. The red dotted curves are the free  $\gamma n \rightarrow \pi^- p$  cross sections from the AO model for the total energy  $W$ .

the calculations to be discussed in this subsection, we find that the results from the dataset (1) of quasi-free process agree with the free cross sections, as expected. In Fig. 13, we show two typical results. The absence of the black solid circles in the forward pion angles is due to the fact that not all pion angles are allowed in the region defined by the kinematical cuts. Thus the results from this dataset (1) of quasi-free process will not be shown in the rest of this subsection.

We first consider the  $d(\gamma, \pi^-)pp$  case. The  $\gamma n \rightarrow \pi^- p$  differential cross sections extracted from using the datasets (2) and (3) are the green triangles and black circles shown in Fig. 14. The differences between these results and the free cross sections (red dotted curves) indicate that the extracted  $d\sigma_{\gamma n}(W)/d\Omega$  contain some FSI effects in the  $E_\gamma < 1000$  MeV region. At higher energies, the FSI effects are very small. In the figure, the  $N$ -exchange FSI effect is visible only at  $E_\gamma = 300$  MeV, and the  $\pi$ -exchange FSI visibly reduces the cross sections in the backward kinematics.

Our results for the  $d(\gamma, \pi^0)pn$  case are shown in Fig. 15. The results from using the datasets (2) (green triangles) and (3) (black solid circles) are not distinguishable at  $E_\gamma = 300$  MeV, indicating the  $\pi$ -exchange FSI can be neglected at energies near the  $\Delta(1232)$  resonance. Clearly, the FSI effects contained in the extracted  $d\sigma_{\gamma n \rightarrow \pi^0 n}(W)/d\Omega$  are rather significant in the  $E_\gamma < 1000$  MeV region. At higher energies  $E_\gamma \geq 1000$  MeV, the FSI effects are weak but still significant in the  $\cos \theta \rightarrow 1$  region, which can be expected from the results shown in Figs. 7 and 8 and the discussion on them. We thus have demonstrated that the

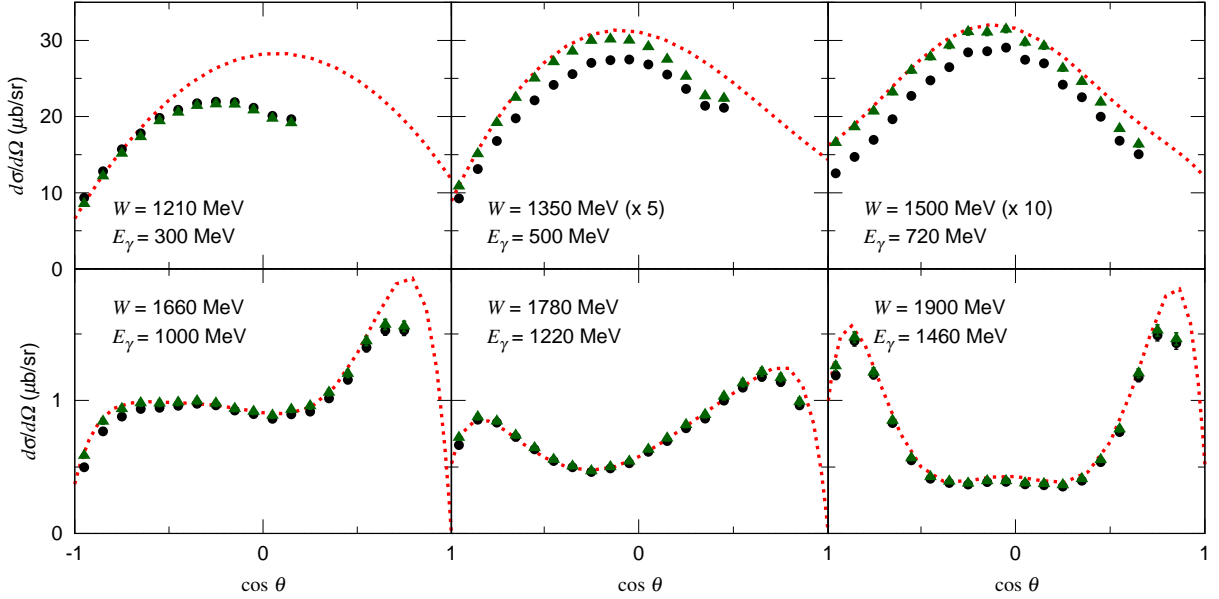


FIG. 15. The pion angular distribution for  $\gamma n \rightarrow \pi^0 n$  extracted from  $d(\gamma, \pi^0)pn$  cross sections. The other features are the same as those in Fig. 14.

FSI effects remain in the extracted  $\gamma n \rightarrow \pi^0 n$  cross sections even the kinematical cuts have been applied.

We note that the  $\pi$ -exchange FSI effect was assumed to be negligible and thus neglected in Ref. [30]. However, the results shown in Fig. 15 clearly show the importance of the  $\pi$ -exchange FSI effect. For example, at  $W = 1500$  MeV, there is a significant overall reduction of the cross sections due to the  $\pi$ -exchange FSI, which is essential in getting agreement with the data [25]. In Ref. [30], on the other hand, the reduction due to the FSI of the  $N$ -exchange is visible only in the forward pion kinematics ( $\cos \theta \gtrsim 0.94$ ) at similar energies.

We have also extracted the  $\gamma p \rightarrow \pi^0 p$  cross sections from similar datasets for  $d(\gamma, \pi^0)pn$ . The results are shown in Fig. 16. By comparing Figs. 15 and 16, the FSI effects on the extractions of  $\gamma n \rightarrow \pi^0 n$  and  $\gamma p \rightarrow \pi^0 p$  cross sections are somewhat different. In general, it could have a few percents difference in the reduction factor defined by the black solid circles divided by the red dotted curves in Figs. 15 and 16. In a previous experimental analysis [25], the FSI for these two extractions were assumed to be the same.

From the above results, it appears that the extractions of unpolarized differential cross sections for  $\gamma N \rightarrow \pi N$  from the data of  $d(\gamma, \pi)NN$  using Eq. (38) and the kinematical cuts listed in Table I are reasonable. However, the FSI effects, in particular for the  $d(\gamma, \pi^0)pn$ , cannot be removed completely. Appropriate corrections must be made in using the  $\gamma n \rightarrow \pi^0 n, \pi^- p$  unpolarized cross sections extracted as above for determining the isospin structure of the nucleon resonances. It is however not trivial to develop a formula to provide the necessary corrections on the extracted results, since the corrections strongly depend on the photon energy  $E_\gamma$ ,  $W$ , pion angle  $\theta$ , and cuts. The use of a dynamical model, such as given in this paper, to evaluate the corrections for each data analysis is perhaps necessary in practice.

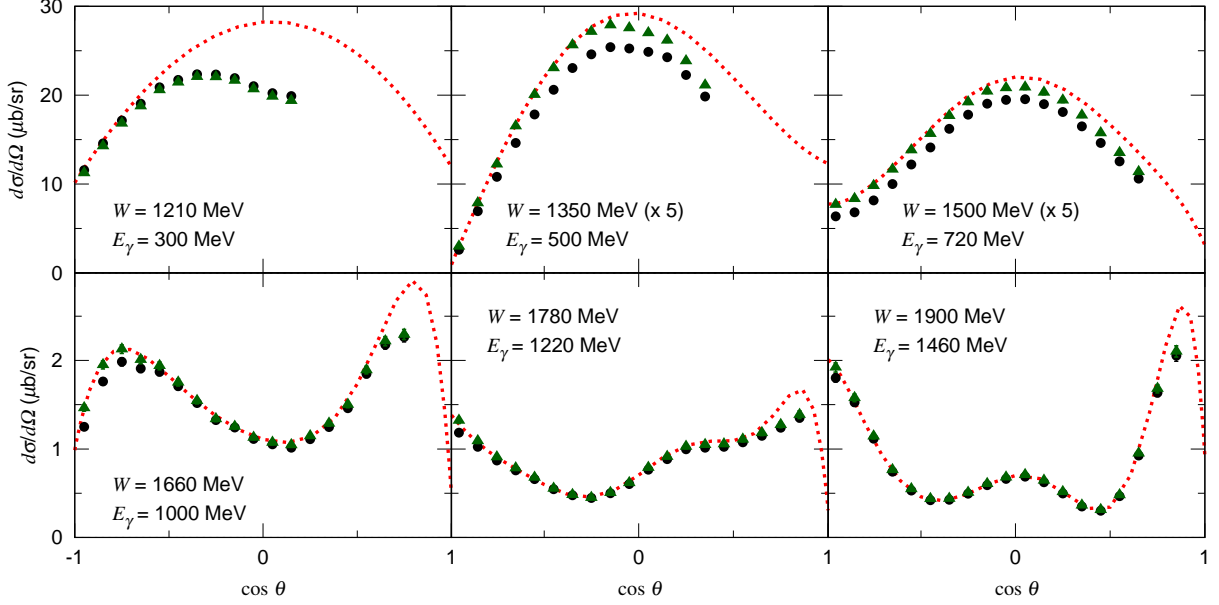


FIG. 16. The pion angular distribution for  $\gamma p \rightarrow \pi^0 p$  extracted from  $d(\gamma, \pi^0)pn$  cross sections. The descriptions of the results are the same as those given in Fig. 14.

## B. Polarization observables

We now investigate the procedures for extracting the polarization observables of  $\gamma N \rightarrow \pi N$  from the data of  $d(\gamma, \pi)NN$ . We will focus on the asymmetries  $\Sigma$ ,  $E$  and  $G$  defined in Sec. II C.

For the quasi-free process, which is given only by the  $t_{f,i}^{\text{imp}}$  of Eq. (7), one can also derive within our formulation a relation between the polarized cross sections of  $\gamma N \rightarrow \pi N$  and  $d(\gamma, \pi)NN$  reactions. However, the simple relation of Eq. (35) is no longer valid because we need to consider the spin rotation of the nucleon due to the transformation from the  $\gamma$ - $d$  frame to  $\gamma$ - $n$  CM frame. To see this, we neglect the deuteron  $d$ -state as we did in deriving Eq. (35), and also set  $\Lambda'_\mu(p_t) \rightarrow \delta'_\mu$  in Eq. (A1) in addition here. By inspecting Eq. (A1), it is easy to see that Eq. (35) can be extended to a case where the initial deuteron spin is polarized to  $s_d = +1$ :

$$\frac{d^2\sigma_{\gamma d}(\lambda, s_d = +1, E_\gamma)}{dW d\cos\theta} = \frac{E'_\gamma}{E_\gamma} \left[ \phi_{1/2,1/2}(W; E_\gamma) \frac{d\sigma_{\gamma N}(\lambda, s_1 = 1/2, W)}{d\cos\theta} + \phi_{-1/2,1/2}(W; E_\gamma) \frac{d\sigma_{\gamma N}(\lambda, s_1 = -1/2, W)}{d\cos\theta} + \dots \right], \quad (40)$$

with [cf. Eq. (36)]

$$\phi_{s_{\bar{e}},s}(W; E_\gamma) = \int d^3p_s \frac{m_N}{E_N(\mathbf{p}_s)} \delta(W - w(\mathbf{p}_s, E_\gamma)) \frac{\rho_d(|\mathbf{p}_s|)}{4\pi} |R_{s_{\bar{e}},s}(p'_1, p_t)|^2, \quad (41)$$

where  $p'_1$  is the momentum of the struck nucleon in the deuteron in the  $\gamma$ - $d$  frame ( $\mathbf{p}'_1 = -\mathbf{p}_s$  in the laboratory frame),  $p_t = p'_1 + q$  is the total momentum of the  $\gamma$ - $N$  system, and  $R_{s_{\bar{e}},s}(p'_1, p_t)$  is the spin rotation matrix defined in Eqs. (A3)-(A4). We have used the fact

that the  $z$ -components of the initial two-nucleon spins must be  $s_1 = s_2 = +1/2$  for  $s_d = +1$ . The last terms on r.h.s. of Eq. (40), which are not explicitly written, are those depend on  $R_{1/2,1/2}(p'_1, p_t)[R_{-1/2,1/2}(p'_1, p_t)]^*$ . Meanwhile, the polarization asymmetry  $E$  for  $\gamma N \rightarrow \pi N$  is defined by

$$E_{\gamma N} = \frac{d\sigma_{\gamma N}(\lambda = 3, s_1 = +1/2, W) - d\sigma_{\gamma N}(\lambda = 4, s_1 = +1/2, W)}{d\sigma_{\gamma N}(\lambda = 3, s_1 = +1/2, W) + d\sigma_{\gamma N}(\lambda = 4, s_1 = +1/2, W)}, \quad (42)$$

where  $\lambda$  has been defined in Eq. (31). Clearly,  $E_{\gamma N}$  cannot be extracted from  $E_{\gamma d}$  of Eq. (30) for the deuteron target alone, which is determined by  $d\sigma_{\gamma d}(\lambda, s_d = +1, E_\gamma)$ , unless the spin rotation matrix element  $R_{-1/2,1/2}(p'_1, p_t)$  of Eq. (41) is negligibly small. What has been done in practice in experimental analyses [22, 28] is to assume the spin rotation negligible, i.e.,  $R_{s'_1, s_1} = \delta_{s'_1, s_1}$ , and use the formula

$$\left. \frac{d^2\sigma_{\gamma d}(\lambda, s_d = +1, E_\gamma)}{dW d\cos\theta} \right|_{\text{cut}} = \phi_{\text{cut}}(W; E_\gamma) \frac{E'_\gamma}{E_\gamma} \frac{d\sigma_{\gamma N}(\lambda, s_1 = +1/2, W)}{d\cos\theta}, \quad (43)$$

where FSI and kinematical cuts have been taken into account. Then the asymmetry  $E_{\gamma N}$  is extracted from the polarized deuteron data by combining Eqs. (42) and (43). Other polarization asymmetries such as  $\Sigma$  and  $G$  for  $\gamma N \rightarrow \pi N$  can also be extracted in a similar manner.

To examine the validity of Eq. (43), we use our model including the impulse +  $N$ -exchange +  $\pi$ -exchange mechanisms to generate data of  $\left. \frac{d^2\sigma_{\gamma d}(\lambda, s_d = +1, E_\gamma)}{dW d\cos\theta} \right|_{\text{cut}}$ , and extract the polarized cross sections  $\frac{d\sigma_{\gamma N}(\lambda, s_1 = 1/2, W)}{d\cos\theta}$  using Eq. (43). The polarization asymmetries  $\Sigma$ ,  $E$ , and  $G$  for  $\gamma N \rightarrow \pi N$  are then calculated and shown in Fig. 17 for  $\gamma n \rightarrow \pi^0 n$  and Fig. 18 for  $\gamma n \rightarrow \pi^- p$ . We find that FSI effects are mostly negligible, and the extracted  $\Sigma$ ,  $E$  and  $G$  for  $\gamma n \rightarrow \pi^0 n, \pi^- p$  agree almost perfectly with the results calculated for the free neutron target. The only exception is a visible difference on  $E$  for  $\gamma n \rightarrow \pi^0 n$  at  $W = 1500$  MeV. Our results thus indicate that the recent polarization data extracted at Mainz [28] are reasonably reliable and can be used to help determine the isospin structure of the nucleon resonances.

### C. Comparison with the previous extractions

We now note that Eq. (38) is the formula with which the cross sections for  $\gamma n \rightarrow \pi N$  at a given  $W$  are extracted from the data of  $d(\gamma, \pi)NN$  at a given  $E_\gamma$ . However, this extraction procedure including the  $W$ -cut was not used in recent experimental analyses of JLab [20, 22, 23] and also in a recent theoretical analysis [29]. The formula used in these analyses can be obtained by first assuming that  $\frac{d\sigma_{\gamma n}(W)}{d\cos\theta}$  in the right-hand side of Eq. (38) is a constant in the range of  $W$  allowed by the kinematical cuts, and then integrating both sides of Eq. (38) over  $W$ . The resulting formula can be written in the following equation

$$\left. \frac{d\sigma_{\gamma d}(E_\gamma)}{d\cos\theta} \right|_{\text{cut}} = \frac{d\sigma_{\gamma n}(\bar{W})}{d\cos\theta} \int dW' \phi_{\text{cut}}(W'; E_\gamma), \quad (44)$$

with

$$\int dW' \phi_{\text{cut}}(W'; E_\gamma) = \int d^3p_s \frac{m_N}{E_N(\mathbf{p}_s)} \frac{E'_\gamma}{E_\gamma} \frac{\rho_d(|\mathbf{p}_s|)}{4\pi} \prod_i \theta(x_i^{\text{max}} - x_i) \theta(x_i - x_i^{\text{min}}), \quad (45)$$

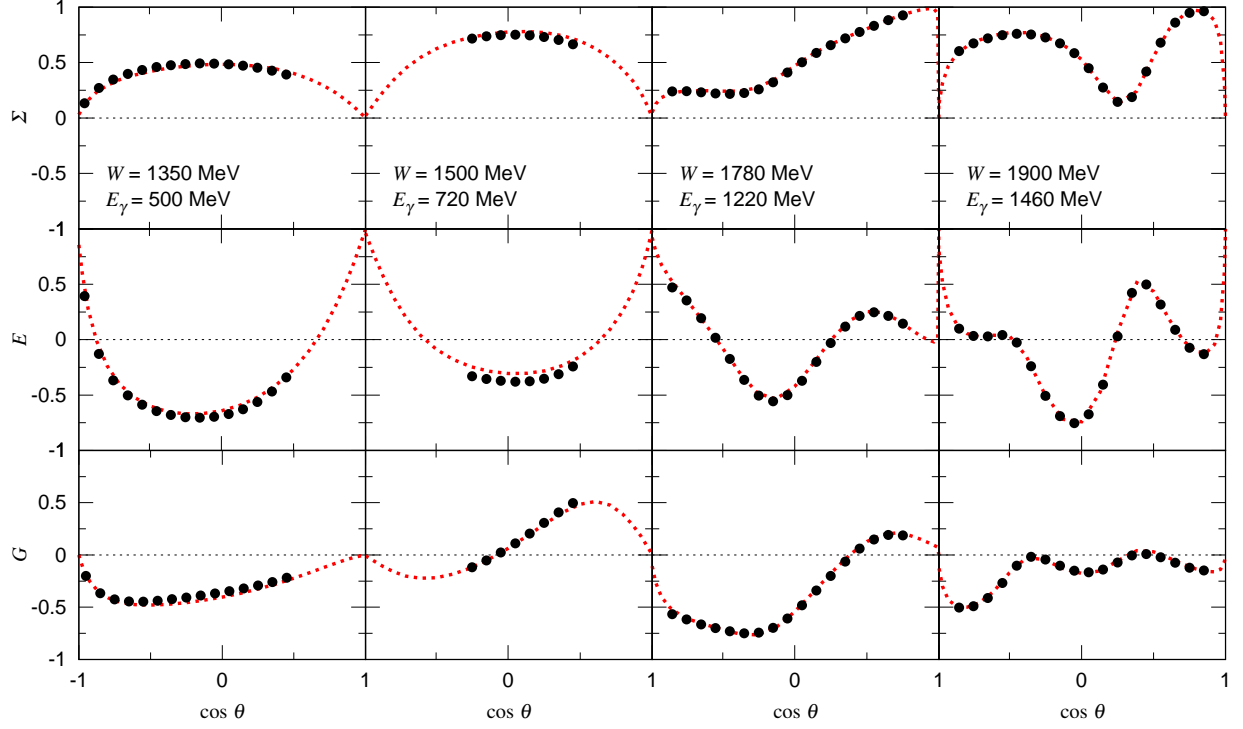


FIG. 17. The polarization observable  $\Sigma$ ,  $E$ , and  $G$  for  $\gamma n \rightarrow \pi^0 n$  extracted from  $d(\gamma, \pi^0)pn$ . The other features are the same as those in Fig. 14.

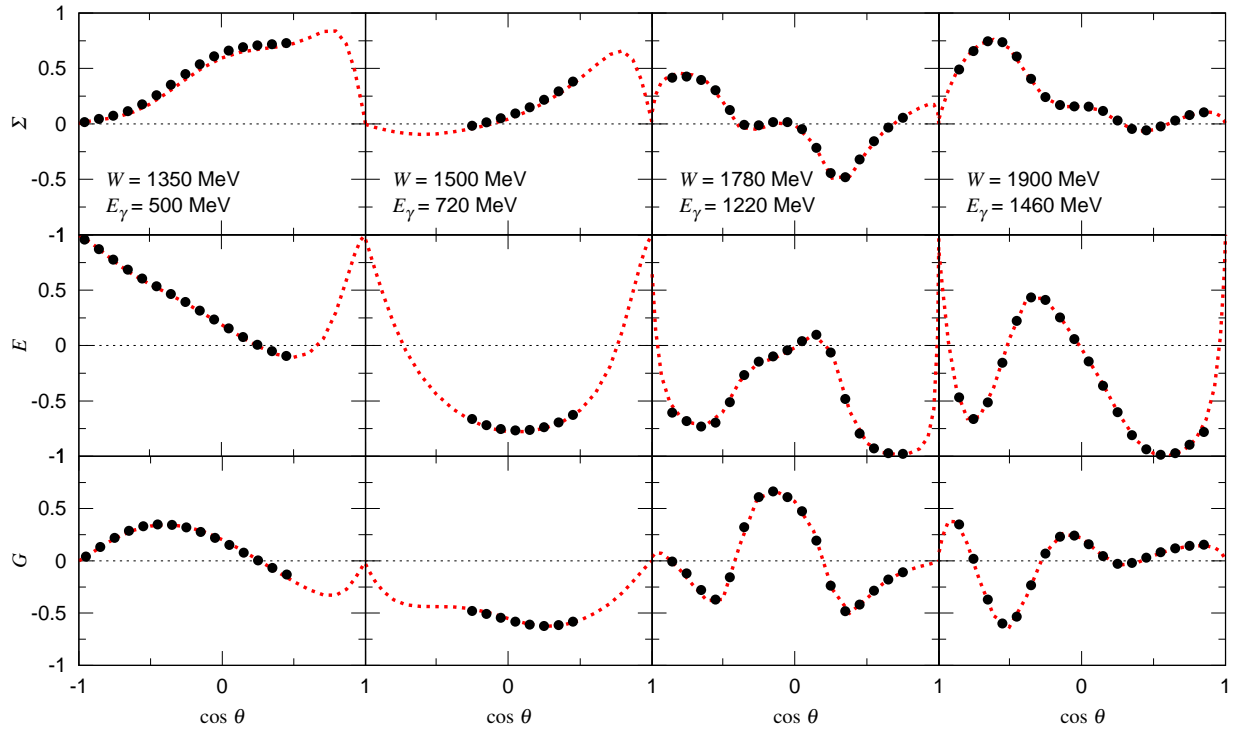


FIG. 18. The polarization observable  $\Sigma$ ,  $E$ , and  $G$  for  $\gamma n \rightarrow \pi^- p$  extracted from  $d(\gamma, \pi^-)pp$ . The other features are the same as those in Fig. 14.

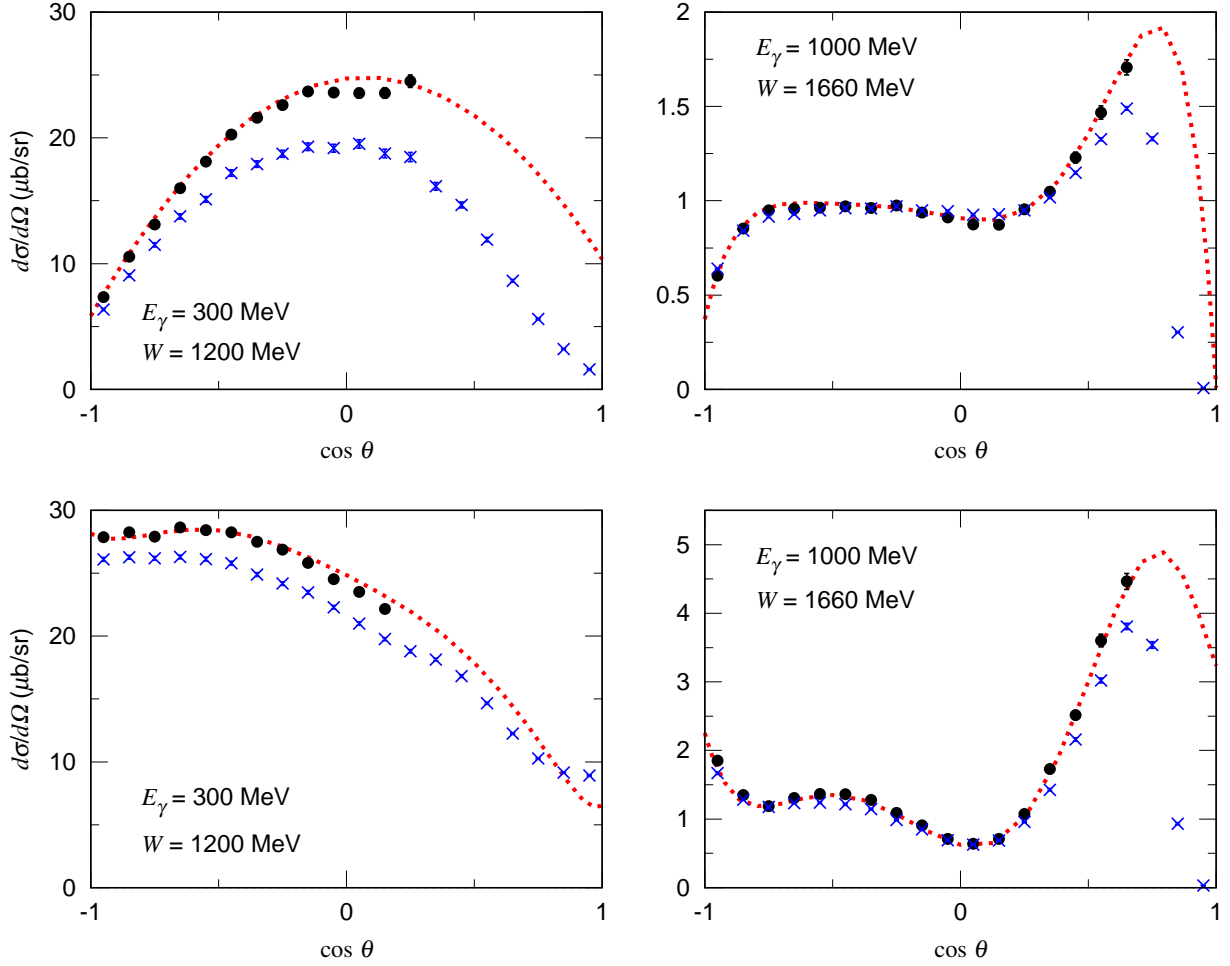


FIG. 19. Upper [Lower] panel: Differential cross sections of  $\gamma n \rightarrow \pi^0 n$  [ $\gamma n \rightarrow \pi^- p$ ] in the CM frame extracted from cross sections for  $d(\gamma, \pi^0)pn$  [ $d(\gamma, \pi^-)pp$ ] including only the quasi-free mechanism. The kinematical cuts used in calculating the  $d(\gamma, \pi)NN$  cross sections are explained in the text. The black circles [blue crosses] are extracted using Eq. (38) [Eq. (44)]. The photon energy ( $E_\gamma$ ) in the  $\gamma$ - $d$  laboratory frame and, for the black circles, the final  $\pi N$  invariant mass ( $W$ ) for  $d(\gamma, \pi)NN_s$  ( $N_s$ : spectator) are indicated in the figure. The red dotted curves are the free  $\gamma n \rightarrow \pi N$  cross sections from the AO model calculated at the total energy  $W$ .

and  $E'_\gamma/E_\gamma = E_N(\mathbf{p}_s)/m_N + \mathbf{p}_s \cdot \hat{\mathbf{q}}_\gamma/m_N$ . The  $\gamma n \rightarrow \pi N$  cross sections obtained with this equation,  $d\sigma_{\gamma n}(\bar{W})/d\cos\theta$ , is an average over a certain range of  $W$  with a certain weight determined by  $E_\gamma$ , the Fermi motion, and the cuts. The invariant mass  $\bar{W}$  for this averaged cross section is usually identified with the invariant mass of the incident photon and a nucleon at rest:  $\bar{W} = \sqrt{2m_N E_\gamma + m_N^2}$ . The use of Eq. (44) is based on the assumption that the average (smearing) due to the Fermi motion does not significantly invalidate this identification. It is therefore informative to investigate the extent to which this assumption is valid within our model.

Considering two typical photon energies at  $E_\gamma = 300, 1000$  MeV, we first calculate  $\left. \frac{d^2\sigma_{\gamma d}(E_\gamma)}{dW d\cos\theta} \right|_{\text{cut}}$  for Eq. (38) and  $\left. \frac{d\sigma_{\gamma d}(E_\gamma)}{d\cos\theta} \right|_{\text{cut}}$  for Eq. (44) from the quasi-free process which is

determined only by the first term  $t_{f,i}^{\text{imp}}$  of Eq. (7). For each photon energy,  $d\sigma_{\gamma n}(W)/d\cos\theta$  at  $W = \bar{W} = \sqrt{2m_N E_\gamma + m_N^2} \simeq 1200$  (1660) MeV for  $E_\gamma = 300$  (1000) MeV is extracted using Eq. (38). Meanwhile,  $d\sigma_{\gamma n}(\bar{W})/d\cos\theta$ , which is an average over a range of  $W \sim 1180 - 1210$  (1600 - 1700) MeV for  $E_\gamma = 300$  (1000) MeV, is extracted using Eq. (44). These two cross sections extracted separately are compared in Fig. 19 with the  $\gamma n \rightarrow \pi^0 n, \pi^- p$  cross sections (red dotted curves) for a free neutron calculated at  $W = \bar{W}$ . We can clearly see that the cross sections (black circles) extracted using Eq. (38), which includes the  $W$ -cut in addition to the cuts in Table I, reproduces very well the free cross sections (red dotted curves), as expected. The absence of the black circles in the forward pion angles is due to the fact that not all the pion angles are allowed by the kinematical cuts specified in Table I plus the  $W$ -cut. On the other hand, Eq. (44), which does not apply the  $W$ -cut to the calculated  $d(\gamma, \pi)NN$  data, includes the data over a much wider kinematical region, and hence the extracted cross sections (blue crosses) can also be obtained in the forward angles.

We next see in Fig. 19 that  $d\sigma_{\gamma n}(\bar{W})/d\cos\theta$  (blue crosses) extracted using Eq. (44) do not always agree well with the free cross sections (red dotted curves). In particular, the extracted cross sections at  $W = 1200$  MeV are significantly lower than the free cross sections in the  $\cos\theta < 0$  region where the results (black circles) are also obtained using Eq. (38) at  $W = \bar{W}$ . This difference can be explained as follows. The  $\gamma n \rightarrow \pi N$  cross sections in the  $W = 1180 - 1210$  MeV region change rapidly and reach the  $\Delta(1232)$  peak near  $W \simeq 1200$  MeV. Because the blue-crosses in Fig. 13 are the values from averaging over this range of  $W$  and hence are necessarily smaller than the free ones at  $W = 1200$  MeV. In the  $\cos\theta \gtrsim 0.3$  region, the black circles are absent, meaning that this region is largely restricted to have  $W = \bar{W} = 1200$  MeV for  $E_\gamma = 300$  MeV by the energy-momentum conservations and the applied kinematical cuts. Therefore, the blue crosses in  $\cos\theta \gtrsim 0.3$  are averages of  $d\sigma_{\gamma n}(W)/d\cos\theta$  of  $W < 1200$  MeV, being significantly different from the free cross sections at  $W = 1200$  MeV.

At  $E_\gamma = 1000$  MeV ( $\bar{W} = 1660$  MeV), on the other hand, there are little differences between three cross sections in the  $\cos\theta < 0.7$  region. This is due to the fact that the free cross sections in the range of  $W \simeq 1600 - 1700$  MeV has a mild and monotonic  $W$ -dependence, and hence an average over it would not be significantly different from the value at  $W = \bar{W}$ . However, in the  $\cos\theta = 0.3 - 0.7$  region, the average does not completely cancel out the  $W$ -dependence of the free cross sections, giving the extracted cross sections (blue crosses) significantly smaller than the free cross sections. This also illustrates a possible difficulty of using Eq. (44).

We also use Eq. (44) without the  $W$ -cut to extract the polarization asymmetries  $\Sigma$ ,  $E$  and  $G$ . Here, we use Cut A (Cut B) of Table I for  $E_\gamma = 300$  (1000) MeV when calculating the  $d(\gamma, \pi)NN$  cross sections. The results (blue crosses) are shown in Figs. 20-21 and are compared with those from using Eq. (43) (black solid circles) and the free neutron results (red dotted curves). Overall, our finding here is very similar to what we found for the unpolarized cross sections presented in Fig. 19. The agreement between the polarization observables extracted with Eq. (43) (black solid circles) and the free ones (red dotted curves) is almost perfect. However, the agreement between the polarization observables (blue crosses) extracted with Eq. (44) without the  $W$ -cut and the free ones is not always good. For example, the extracted  $G$  for  $\gamma n \rightarrow \pi^- p$  shown in the lower row of Fig. 21 is rather different from the free one. The difference again stems from averaging a rapid and non-monotonic  $W$ -dependence of  $G$  for the free  $\gamma n \rightarrow \pi^- p$  around  $W = 1660$  MeV. The asymmetry  $E$  for  $\gamma n \rightarrow \pi^- p$  shown in the upper row of Fig. 21 also significantly deviates from the free

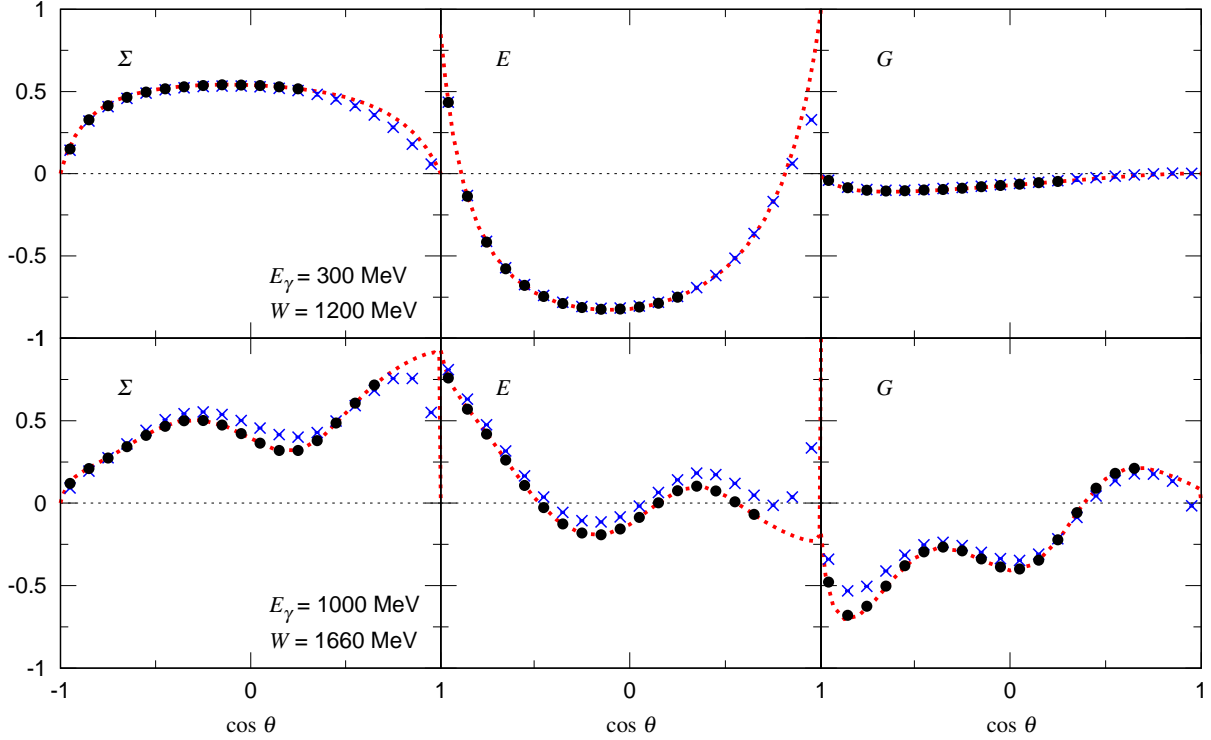


FIG. 20. The polarization observables ( $\Sigma, E, G$ ) for  $\gamma n \rightarrow \pi^0 n$  extracted from  $d(\gamma, \pi^0)pn$  cross sections. The kinematical cuts used in calculating the  $d(\gamma, \pi)NN$  cross sections are Cut A (Cut B) of Table I for  $E_\gamma = 300$  (1000) MeV. Otherwise the description of the result is the same as given in Fig. 19.

one in  $\cos \theta \gtrsim 0$ . In these pion angles,  $\gamma n \rightarrow \pi^- p$  at  $W \sim 1200$  MeV in the deuteron are mostly eliminated by the kinematical cuts, as indicated by the absence of the black circles, and  $\gamma n \rightarrow \pi^- p$  of  $W \sim 1120 - 1180$  MeV mainly contribute here. The average over this range of  $W$  gives the blue crosses in the figure which deviates significantly from the free  $E$  of  $W = 1200$  MeV.

Summarizing, our results shown in Figs. 19-21 indicate that the Fermi smearing can be a problematic effect when Eq. (44) is used for extracting the neutron target observables, and that the  $\gamma n \rightarrow \pi N$  data extracted without the  $W$ -cut should be corrected appropriately.

## V. SUMMARY AND FUTURE DEVELOPMENTS

We have investigated the  $d(\gamma, \pi)NN$  by using a dynamical model of  $\pi N$  and  $\gamma N$  reactions in the nucleon resonance region. Within the multiple scattering formulation, the calculations of the cross sections of  $d(\gamma, \pi)NN$  reactions include the impulse term and the final-state interaction terms due to the pion-exchange and nucleon-exchange mechanisms. The predicted differential cross sections are in good agreement with most of the available data of  $d(\gamma, \pi^0)np$  and  $d(\gamma, \pi^-)pp$  reactions. We showed that the off-shell effects, calculated from the meson-exchange mechanisms, on the propagations of the exchanged nucleon and pion are significant in determining the reaction amplitudes. The FSI effects on the predicted

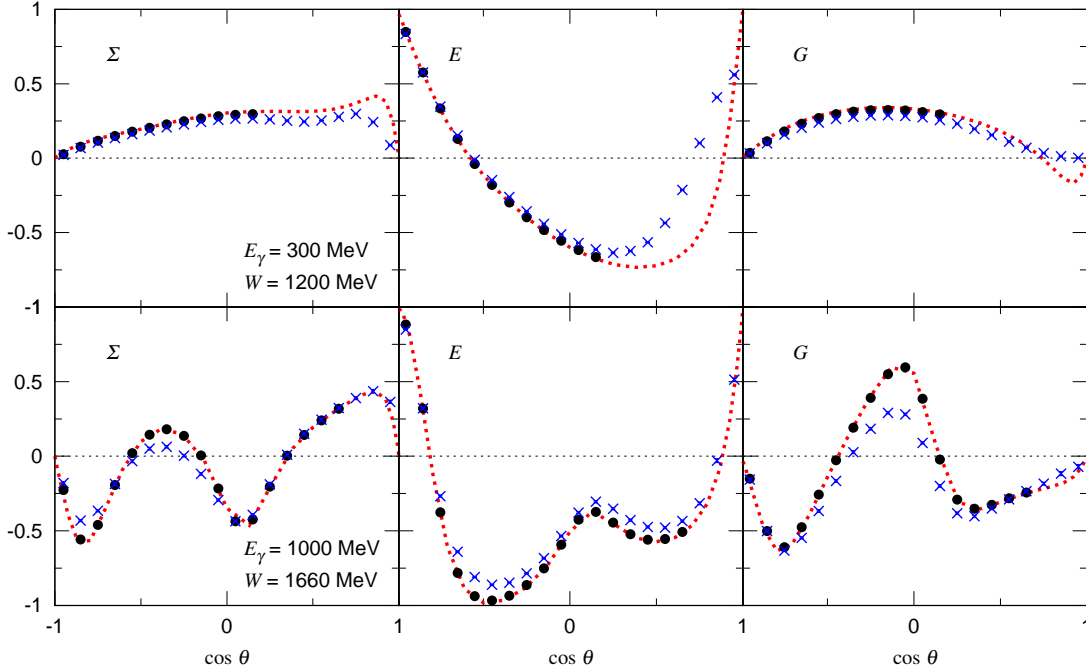


FIG. 21. The polarization observables ( $\Sigma, E, G$ ) for  $\gamma n \rightarrow \pi^- p$  extracted from  $d(\gamma, \pi^-)pp$  cross sections. The description of the result is the same as given in Fig. 20.

cross sections are found to be important at energies near the  $\Delta(1232)$  resonance, and are still significant at higher energies.

We used our model to examine a commonly used procedure for extracting the (un)polarized  $\gamma n \rightarrow \pi N$  observables from the  $d(\gamma, \pi)NN$  data. We find that the extractions of unpolarized differential cross sections of  $\gamma N \rightarrow \pi N$  from the data of  $d(\gamma, \pi)NN$  using Eq. (38) combined with the kinematical cuts listed in Table I are fairly reasonable. However, the FSI effects, in particular for the  $d(\gamma, \pi^0)pn$ , cannot be removed completely. Appropriate corrections must be made in using the extracted  $\gamma n \rightarrow \pi^0 n, \pi^- p$  unpolarized cross sections for determining the isospin structure of the nucleon resonances. It is however not trivial to develop a formula giving the necessary corrections on the extracted results, since the corrections depend strongly on the photon energy  $E_\gamma$ ,  $W$ , scattering angles, and kinematical cuts. The use of a dynamical model, such as presented in this paper, to evaluate the corrections for each data analysis is perhaps necessary in practice. We have also examined an extraction procedure using Eq. (44) in which the  $W$ -cut is not included. This procedure has been taken recently by experimental analyses in JLab [20, 22, 23] and also in a recent theoretical analysis [29]. We found that (un)polarized  $\gamma n \rightarrow \pi N$  cross sections extracted with Eq. (44) can be rather different from the free neutron observables because of the Fermi smearing effect. We confirmed that the  $W$ -cut very efficiently suppress the Fermi smearing effect, leading to a very accurate extraction up to the FSI effects.

For studying the nucleon resonances, it will be most desirable to determine the multipole amplitudes for  $\gamma n \rightarrow \pi^0 n, \pi^- p$  by directly fitting the data of  $d(\gamma, \pi)NN$ . However, this is not computationally practical for the dynamical model presented in this paper. Instead, we can make a progress by combining the procedure with kinematical cuts, as investigated in

this work, and the dynamical model calculations as follows:

1. Start with a certain set of parameters of a dynamical model that generates  $\gamma n \rightarrow \pi N$  amplitudes. Implement the amplitudes in a dynamical  $d(\gamma, \pi)NN$  reaction model.
2. With the same set of kinematical cuts as used in an experiment, calculate  $\frac{d^2\sigma_{\gamma d}}{dW d\cos\theta}\Big|_{\text{cut}}$  with the dynamical  $d(\gamma, \pi)NN$  reaction model including the FSI, and extract  $\frac{d\sigma_{\gamma n}(W)}{d\cos\theta}$  using Eq. (38). By comparing the extracted  $\gamma n \rightarrow \pi N$  cross sections with the free ones from the  $\gamma n \rightarrow \pi N$  amplitudes built in the  $\gamma d$  model, the FSI correction factor on the extracted cross sections is obtained.
3. Substitute experimental data into the l.h.s. of Eq. (38) and obtain  $\frac{d\sigma_{\gamma n}(W)}{d\cos\theta}$  in the r.h.s. of the equation. The obtained quantity is further applied by the FSI correction factor from the previous step, then data for  $\gamma n \rightarrow \pi N$  cross sections are extracted.
4. Calculate  $\gamma n \rightarrow \pi N$  cross sections with the elementary amplitudes that have been built in the  $\gamma d$  model, and compare them with the experimental data extracted in the previous step. If they agree, the extraction of the  $\gamma n \rightarrow \pi N$  experimental data as well as that of the corresponding amplitudes are completed. If not, fit the data by adjusting the parameters of the dynamical model for the  $\gamma n \rightarrow \pi N$  amplitudes, and then return to the step 1.

## ACKNOWLEDGMENTS

We thank W.N. Polyzou for his assistance to the use of their relativistic reaction theory. We also thank A. Sandorfi, T. Kageya, D. Carman, B. Krusche, and M. Dieterle for useful information on their experimental data and encouragements. This work is in part supported by Fundação de Amparo à Pesquisa do Estado de São Paulo (FAPESP), Process No. 2016/15618-8, by JSPS KAKENHI Grant Numbers 25105010 and 16K05354, and by the U.S. Department of Energy, Office of Science, Office of Nuclear Physics, Contract No. DE-AC02-06CH11357. Numerical computations in this work were carried out with SR16000 at YITP in Kyoto University, the High Performance Computing system at RCNP in Osaka University, the National Energy Research Scientific Computing Center, which is supported by the Office of Science of the U.S. Department of Energy under Contract No. DE-AC02-05CH11231, and the use of the Bebop [or Blues] cluster in the Laboratory Computing Resource Center at Argonne National Laboratory.

## Appendix A: Ingredients for $\gamma d \rightarrow \pi N_1 N_2$ matrix elements in Eqs. (8)-(10)

The off-energy-shell two-body matrix elements for calculating Eqs. (8)-(10) are defined in the  $\gamma$ - $d$  laboratory frame. Here we give formulas for getting these matrix elements from the matrix elements in the CM frame of  $\gamma N$ ,  $\pi N$ , and  $NN$  systems. Our formula are derived from using the procedures of Refs. [41, 42] within the instant form of relativistic quantum mechanics [43]. The details of this approach can be found in these references. Here we only give the formulas used in our numerical calculations.

### 1. $\gamma N \rightarrow \pi N'$ matrix elements

The off-shell  $\gamma N \rightarrow \pi N'$  matrix element  $\langle \pi N' | t_{\pi N, \gamma N}(W) | \gamma N \rangle$  in Eqs. (8)-(10), is related to those evaluated in the CM frame of  $\pi N'$  by

$$\begin{aligned}
& \langle \pi(\mathbf{k}, t_\pi) N'(\mathbf{p}', s', t') | t_{\pi N, \gamma N}(W) | \gamma(\mathbf{q}, \lambda) N(\mathbf{p}, s, t) \rangle \\
&= \langle \pi(\mathbf{k}, t_\pi) N'(\mathbf{p}', s', t') | \epsilon_\lambda^\mu(q) [j(W)]_\mu | N(\mathbf{p}, s, t) \rangle \\
&= \sqrt{\frac{|\mathbf{q}_{\bar{c}}| E_\pi(\mathbf{k}_{\bar{c}}) E_N(-\mathbf{q}_{\bar{c}}) E_N(-\mathbf{k}_{\bar{c}})}{|\mathbf{q}| E_\pi(\mathbf{k}) E_N(\mathbf{p}) E_N(\mathbf{p}')}} \sum_{\mu\nu} \epsilon_\lambda^\mu(q) \Lambda_\mu^\nu(p_t) \sum_{s_{\bar{c}}, s'_{\bar{c}}} R_{s'_{\bar{c}}, s'}^*(p', p_t) R_{s_{\bar{c}}, s}(p, p_t) \\
&\times \langle \pi(\mathbf{k}_{\bar{c}}, t_\pi) N'(-\mathbf{k}_{\bar{c}}, s'_{\bar{c}}, t') | [j_{\bar{c}}(W)]_\nu | N(-\mathbf{q}_{\bar{c}}, s_{\bar{c}}, t) \rangle, \tag{A1}
\end{aligned}$$

where the suffixes ' $\bar{c}$ ' indicate quantities in the CM system of  $\pi N'$ ,  $\epsilon_\lambda^\mu(q)$  is the photon polarization vector,  $j_\mu(W)$  is the current operator,  $p_t = p' + k$  is a four-momentum defined by  $\mathbf{p}_t = \mathbf{p}' + \mathbf{k}$  and  $p_t^0 = E_N(\mathbf{p}') + E_\pi(\mathbf{k})$ . The CM matrix elements of the current operator,  $\langle \pi(\mathbf{k}_{\bar{c}}, t_\pi) N'(-\mathbf{k}_{\bar{c}}, s'_{\bar{c}}, t') | [j_{\bar{c}}(W)]_\mu | N(-\mathbf{q}_{\bar{c}}, s_{\bar{c}}, t) \rangle$ , from the ANL-Osaka model are calculated following the procedure detailed in Appendix D of Ref. [18], and their normalization is specified by Eq. (D2) of the reference.

In Eq. (A1), the quantity  $\Lambda_\mu^\nu(p_t)$  boosts the CM momenta  $a_{\bar{c}} = (k_{\bar{c}}^0, \mathbf{k}_{\bar{c}}) [(q_{\bar{c}}^0, \mathbf{q}_{\bar{c}})]$  to the Lab momenta  $a_L = (k^0, \mathbf{k}) [(q^0, \mathbf{q})]$  by the Lorentz transformation,

$$\begin{aligned}
a_L^0 &= \sum_\nu \Lambda_\nu^0(p_t) a_{\bar{c}}^\nu = \frac{a_{\bar{c}}^0 p_t^0 + \mathbf{p}_t \cdot \mathbf{a}_{\bar{c}}}{m_t}, \\
a_L^i &= \sum_\nu \Lambda_\nu^i(p_t) a_{\bar{c}}^\nu = a_{\bar{c}}^i + p_t^i \left[ \frac{\mathbf{p}_t \cdot \mathbf{a}_{\bar{c}}}{m_t(m_t + p_t^0)} + \frac{a_{\bar{c}}^0}{m_t} \right], \tag{A2}
\end{aligned}$$

where the index  $i = 1, 2, 3$  is a spatial component and  $m_t \equiv \sqrt{\mathbf{p}_t \cdot \mathbf{p}_t}$ .

The spin rotation matrix  $R_{s_{\bar{c}}, s}(p, p_t)$  in Eq. (A1) is given [41, 42] explicitly as:

$$R_{s_{\bar{c}}, s}(p, p_t) = \langle s_{\bar{c}} | B^{-1}(p_{\bar{c}}/m_N) B^{-1}(p_t/m_t) B(p/m_N) | s \rangle, \tag{A3}$$

where  $|s_{\bar{c}}\rangle$  is the spin state of the nucleon,  $p_{\bar{c}}$  is obtained from the nucleon momentum  $p$  in the laboratory frame by the Lorentz transformation of Eq. (A2), and

$$\begin{aligned}
B(p/m) &= \frac{1}{\sqrt{2m(p^0 + m)}} ((p^0 + m)\mathbb{1} + \mathbf{p} \cdot \boldsymbol{\sigma}), \\
B^{-1}(p/m) &= \frac{1}{\sqrt{2m(p^0 + m)}} ((p^0 + m)\mathbb{1} - \mathbf{p} \cdot \boldsymbol{\sigma}), \tag{A4}
\end{aligned}$$

where  $\boldsymbol{\sigma}$  is the Pauli operator and  $\mathbb{1}$  is the unit matrix.

### 2. $\pi' N' \rightarrow \pi N$ matrix element

The half-off-shell  $\pi' N' \rightarrow \pi N$  scattering amplitudes in the laboratory frame, appearing in Eq. (10), are related to those in the  $\pi N$  CM frame by

$$\begin{aligned}
& \langle \pi(\mathbf{k}, t_\pi) N(\mathbf{p}, s, t) | t_{\pi N}(M_{\pi N}) | \pi'(\mathbf{k}', t'_\pi) N'(\mathbf{p}', s', t') \rangle \\
&= \sqrt{\frac{E_\pi(\mathbf{k}_{\bar{c}}) E_N(-\mathbf{k}_{\bar{c}}) E_\pi(\mathbf{k}'_{\bar{c}}) E_N(-\mathbf{k}'_{\bar{c}})}{E_\pi(\mathbf{k}) E_N(\mathbf{p}) E_\pi(\mathbf{k}') E_N(\mathbf{p}')}} \sum_{s_{\bar{c}}, s'_{\bar{c}}} R_{s_{\bar{c}}, s}^*(p, p_t) R_{s'_{\bar{c}}, s'}(p', p_t) \\
&\times \langle \pi(\mathbf{k}_{\bar{c}}, t_\pi) N(-\mathbf{k}_{\bar{c}}, s_{\bar{c}}, t) | t_{\pi N}^{\bar{c}}(M_{\pi N}) | \pi'(\mathbf{k}'_{\bar{c}}, t'_\pi) N'(-\mathbf{k}'_{\bar{c}}, s'_{\bar{c}}, t') \rangle, \tag{A5}
\end{aligned}$$

where the momentum  $\mathbf{k}_{\bar{c}}$  in the  $\pi N$  CM frame is related to  $\mathbf{k}$  in the laboratory frame by the Lorentz transformation Eq. (A2). Here we choose  $\mathbf{p}_t = \mathbf{k} + \mathbf{p}$  and  $p_t^0 = E_\pi(\mathbf{k}) + E_N(\mathbf{p})$ . Within our formulation where an energy of a particle  $x$  is always related to its off-shell momentum ( $\mathbf{p}_x$ ) by  $E_x = \sqrt{|\mathbf{p}_x|^2 + m_x^2}$ , the same Lorentz transformation does not bring the off-shell  $\pi'N'$  system in the laboratory frame into their CM frame. Therefore, we define the  $\pi'N'$  relative momentum in the  $\pi N$  CM frame by  $\mathbf{k}'_{\bar{c}} = (m_N \tilde{\mathbf{k}}'_{\bar{c}} - m_\pi \tilde{\mathbf{p}}'_{\bar{c}})/(m_N + m_\pi)$ , where  $\tilde{\mathbf{k}}'_{\bar{c}}$  and  $\tilde{\mathbf{p}}'_{\bar{c}}$  are related to  $\mathbf{k}'$  and  $\mathbf{p}'$  by the same Lorentz transformation Eq. (A2). The  $\pi N$  scattering amplitudes in the  $\pi N$  CM frame,  $\langle \pi(\mathbf{k}_{\bar{c}}, t_\pi) N(-\mathbf{k}_{\bar{c}}, s_{\bar{c}}, t) | T_{\pi N}^{\bar{c}}(M_{\pi N}) | \pi'(\mathbf{k}'_{\bar{c}}, t'_\pi) N'(-\mathbf{k}'_{\bar{c}}, s'_{\bar{c}}, t') \rangle$ , are calculated following the procedure detailed in Appendix C of Ref. [18], and their normalization is specified by Eq. (C7) of the reference.

### 3. $N'_1 N'_2 \rightarrow N_1 N_2$ matrix element

The half off-shell  $N'_1 N'_2 \rightarrow N_1 N_2$  matrix elements in the laboratory frame, appearing in Eq. (9), are related to those in the  $N_1 N_2$  CM frame by

$$\begin{aligned} & \langle N_1(\mathbf{p}_1, s_1, t_1) N_2(\mathbf{p}_2, s_2, t_2) | T_{NN}(M_{N_1 N_2}) | N'_1(\mathbf{p}'_1, s'_1, t_1) N'_2(\mathbf{p}'_2, s'_2, t_2) \rangle \\ &= \sqrt{\frac{E_N^2(\mathbf{p}_{\bar{c}}) E_N^2(\mathbf{p}'_{\bar{c}})}{E_N(\mathbf{p}_1) E_N(\mathbf{p}_2) E_N(\mathbf{p}'_1) E_N(\mathbf{p}'_2)}} \sum_{s_{1\bar{c}}, s_{2\bar{c}}, s'_{1\bar{c}}, s'_{2\bar{c}}} R_{s_{1\bar{c}}, s_1}^*(p_1, p_t) R_{s_{2\bar{c}}, s_2}^*(p_2, p_t) R_{s'_{1\bar{c}}, s'_1}(p'_1, p_t) R_{s'_{2\bar{c}}, s'_2}(p'_2, p_t) \\ & \times \langle N_1(\mathbf{p}_{\bar{c}}, s_{1\bar{c}}, t_1) N_2(-\mathbf{p}_{\bar{c}}, s_{2\bar{c}}, t_2) | T_{NN}^{\bar{c}}(M_{N_1 N_2}) | N'_1(\mathbf{p}'_{\bar{c}}, s'_{1\bar{c}}, t_1) N'_2(-\mathbf{p}'_{\bar{c}}, s'_{2\bar{c}}, t_2) \rangle, \end{aligned} \quad (\text{A6})$$

with  $p_t$  being  $\mathbf{p}_t = \mathbf{p}_1 + \mathbf{p}_2$  and  $p_t^0 = E_N(\mathbf{p}_1) + E_N(\mathbf{p}_2)$ . Regarding the  $NN$  relative momenta, we use the non-relativistic relation  $\mathbf{p}_{\bar{c}} = (\mathbf{p}_1 - \mathbf{p}_2)/2$  and  $\mathbf{p}'_{\bar{c}} = (\mathbf{p}'_1 - \mathbf{p}'_2)/2$ . The  $NN$   $T$ -matrix  $\langle T_{NN}^{\bar{c}} \rangle$  is expanded in terms of partial waves as

$$\begin{aligned} & \langle N_1(\mathbf{p}_{\bar{c}}, s_{1\bar{c}}, t_1) N_2(-\mathbf{p}_{\bar{c}}, s_{2\bar{c}}, t_2) | T_{NN}^{\bar{c}}(M_{N_1 N_2}) | N'_1(\mathbf{p}'_{\bar{c}}, s'_{1\bar{c}}, t_1) N'_2(-\mathbf{p}'_{\bar{c}}, s'_{2\bar{c}}, t_2) \rangle \\ &= \sum_{JLL'ST} \left( \frac{1 - (-1)^{L+S+T}}{2^{|t_1+t_2|}} \right) \sum_{S^z S'^z L^z L'^z J^z T^z} t_{NN}^{JLL'ST}(|\mathbf{p}_{\bar{c}}|, |\mathbf{p}'_{\bar{c}}|; M_{N_1 N_2}) \\ & \times (1/2, t_1, 1/2, t_2 | TT^z) (1/2, s_{1\bar{c}}, 1/2, s_{2\bar{c}} | SS^z) (LL^z SS^z | JJ^z) Y_{LL^z}(\hat{\mathbf{p}}_{\bar{c}}) \\ & \times (1/2, t_1, 1/2, t_2 | TT^z) (1/2, s'_{1\bar{c}}, 1/2, s'_{2\bar{c}} | SS'^z) (L'L'^z SS'^z | JJ^z) Y_{L'L'^z}^*(\hat{\mathbf{p}}'_{\bar{c}}), \end{aligned} \quad (\text{A7})$$

where  $t_{NN}^{JLL'ST}$  is a partial wave  $NN$  amplitude characterized by the quantum numbers  $JLL'ST$  meaning of which are self-evident in the above equation. On- and off-shell partial wave  $NN$  amplitudes are obtained by solving the following Lippmann-Schwinger equation:

$$t_{NN}^{JLL'ST}(p, p'; M_{N_1 N_2}) = v_{NN}^{JLL'ST}(p, p') + \sum_{L''} \int_0^\infty q^2 dq \frac{v_{NN}^{JLL''ST}(p, q) t_{NN}^{JL''L'ST}(q, p'; M_{N_1 N_2})}{M_{N_1 N_2} - 2m_N - \frac{q^2}{m_N} + i\epsilon}, \quad (\text{A8})$$

where we use the CD-Bonn potential [38] for  $v_{NN}^{JLL'ST}(p', p)$ .

#### 4. Deuteron wave function

The deuteron wave function in its rest frame, appearing in Eqs. (8)-(10), is more explicitly written as

$$\langle N_1(\mathbf{p}, s_1, t_1) N_2(-\mathbf{p}, s_2, t_2) | \Psi_d(s_d) \rangle = \left[ \frac{\delta_{s_s, s_d}}{\sqrt{4\pi}} u_s(p) + (2, s_d - s, 1, s | 1s_d) u_d(p) Y_{2, s_d - s}(\hat{p}) \right] \times (1/2, s_1, 1/2, s_2 | 1s)(1/2, t_1, 1/2, t_2 | 00), \quad (\text{A9})$$

with  $s = s_1 + s_2$ . The radial  $s$ - and  $d$ -wave functions, denoted by  $u_s$  and  $u_d$  respectively, are normalized as  $\int_0^\infty dp p^2 (|u_s(p)|^2 + |u_d(p)|^2) = 1$ . We use the CD-Bonn potential [38] to generate the deuteron wave function. The nucleon momentum distribution in the deuteron is given by

$$\rho_d(p) = |u_s(p)|^2 + |u_d(p)|^2. \quad (\text{A10})$$

- 
- [1] See review by R. Machleidt in *Advance in Nuclear Physics*, edited by J.W. Negele and E. Vogt (Pleum, New York, 1989), Chap.2 Vol. 19.
  - [2] See review by A. Donnachie in *High Energy Physics*, edited by E. Burhop (Academic Press, New York, 1972), Vol.5, P.1.
  - [3] See review by S. Capstick and W. Robert, *Prog. Part. Nucl. Phys.* **45**, S241-S331 (2000).
  - [4] T. Sato and T.-S.H. Lee, *Phys. Rev. C* **54**, 2660 (1996); **63**, 055201 (2001).
  - [5] A. Matsuyama, T. Sato, and T.-S.H. Lee, *Phys. Rept* **439**, 193 (2007).
  - [6] L. Alvarez-Ruso, Y. Hayato, and J. Nieves, *New J. Phys.* **16**, 075015 (2014); S.X. Nakamura et al., *Rept. Prog. Phys.* **80**, 056301 (2017); L. Alvarez-Ruso et al., arXiv:1706.03621 [hep-ph].
  - [7] B. Julia-Diaz, T.-S.H. Lee, A. Matsuyama, and T. Sato, *Phys. Rev. C* **76**, 065201 (2007).
  - [8] B. Julia-Diaz, T.-S.H. Lee, A. Matsuyama, T. Sato, and L.C. Smith, *Phys. Rev. C* **77**, 045201 (2008).
  - [9] J. Durand, B. Julia-Diaz, T.-S.H. Lee, B. Saghai, and T. Sato, *Phys. Rev. C* **78**, 025204 (2008).
  - [10] N. Suzuki, T. Sato, and T.-S.H. Lee, *Phys. Rev. C* **79**, 025205 (2009).
  - [11] H. Kamano, B. Julia-Diaz, T.-S.H. Lee, A. Matsuyama, T. Sato, *Phys. Rev. C* **79**, 025206 (2009).
  - [12] B. Julia-Diaz, H. Kamano, T.-S.H. Lee, A. Matsuyama, T. Sato, and N. Suzuki, *Phys. Rev. C* **80**, 025207 (2009).
  - [13] H. Kamano, B. Julia-Diaz, T.-S.H. Lee, A. Matsuyama, T. Sato, *Phys. Rev. C* **80**, 065203 (2009).
  - [14] N. Suzuki, B. Julia-Diaz, H. Kamano, T.-S.H. Lee, A. Matsuyama, and T. Sato, *Phys. Rev. Lett.* **104**, 042302 (2010).
  - [15] H. Kamano, S.X. Nakamura, T.-S.H. Lee, and T. Sato, *Phys. Rev. C* **81**, 065207 (2010).
  - [16] N. Suzuki, T. Sato, and T.-S.H. Lee, *Phys. Rev. C* **82**, 045206 (2010).
  - [17] A. Sandorfi, S. Hoblit, H. Kamano, and T.-S.H. Lee, *J. Phys. G* **38**, 053001 (2011).
  - [18] H. Kamano, S.X. Nakamura, T.-S.H. Lee, and T. Sato, *Phys. Rev. C* **88**, 035209 (2013).
  - [19] H. Kamano, S.X. Nakamura, T.-S.H. Lee, and T. Sato, *Phys. Rev. C* **94**, 015201 (2016).

- [20] W.J. Briscoe, A.E. Kudryavtsev, P. Pedroni, I.I. Strakovsky, V.E. Tarasov, and R.L. Workman, *Phys. Rev. C* **86**, 065207 (2012).
- [21] W. Chen, H. Gao, W.J. Briscoe, D. Dutta, A.E. Kudryavtsev, M. Mirazita, M. Paris, P. Rossi, S. Stepanyan, I.I. Strakovsky, V.E. Tarasov, and R.L. Workman, *Phys. Rev. C* **86**, 015206 (2012); W. Chen et al. (CLAS Collaboration), *Phys. Rev. Lett.* **103**, 012301 (2009).
- [22] D. Ho et al. (CLAS Collaboration), *Phys. Rev. Lett.* **118**, 242002 (2017).
- [23] P.T. Mattione et al. (CLAS Collaboration), *Phys. Rev. C* **96**, 035204 (2017).
- [24] D. Werthmüller et al. (A2 Collaboration), *Phys. Rev. Lett.* **111**, 232001 (2013).
- [25] M. Dieterle et al. (A2 Collaboration), *Phys. Rev. Lett.* **112**, 142001 (2014).
- [26] D. Werthmüller et al. (A2 Collaboration), *Phys. Rev. C* **90**, 015205 (2014).
- [27] L. Witthauer et al. (A2 Collaboration), *Phys. Rev. C* **95**, 055201 (2017).
- [28] M. Dieterle et al., *Phys. Lett.* **B770**, 523 (2017).
- [29] V.E. Tarasov, W.J. Briscoe, H. Gao, A.E. Kudryavtsev, and I.I. Strakovsky, *Phys. Rev. C* **84**, 035203 (2011).
- [30] V.E. Tarasov, W.J. Briscoe, M. Dieterle, B. Krusche, A.E. Kudryavtsev, M. Ostrick, and I.I. Strakovsky, *Phys. Atom. Nucl.* **79**, 216 (2016).
- [31] T. Sato, M. Kobayashi, and H. Ohtsubo, *Prog. Theor. Phys.* **98**, 927 (1997).
- [32] H. Feshbach, *Theoretical Nuclear Physics, Nuclear Reactions* (Wiley, New York, 1992); A.K. Kerman, H. McManus, and R.M. Thaler, *Ann. Phys.* **8**, 551 (1959).
- [33] E.M. Darwish, H. Arenhövel and M. Schwamb, *Eur. Phys. J.* **A16**, 111 (2003).
- [34] A. Fix and H. Arenhövel, *Phys. Rev. C* **72**, 064005 (2005).
- [35] M.I. Levchuk, A.Yu. Loginov, A.A. Sidorov, V.N. Stibunov and M. Schumacher, *Phys. Rev. C* **74**, 014004 (2006).
- [36] M. Schwamb, *Phys. Rep.* **485**, 109 (2010).
- [37] J.-J. Wu, T. Sato, and T.-S.H. Lee, *Phys. Rev. C* **91**, 035203 (2015).
- [38] R. Machleidt, *Phys. Rev. C* **63**, 024001 (2001).
- [39] A.W. Thomas and R.H. Landau, *Phys. Rept.* **58**, 121 (1980).
- [40] T.-S.H. Lee, *Phys. Lett* **67B**, 282 (1977).
- [41] W.N. Polyzou and Ch. Elster, *J. Phys. G* **41**, 094006 (2014); W.N. Polyzou, W. Glöckle, and H. Witała, *Few Body Syst.* **56**, 395 (2015).
- [42] W. N. Polyzou, private communication.
- [43] See review by B.D. Keidster and W.N. Polyzou in *Advance in Nuclear Physics*, by J.W. Negele and E. Vogt (Plenum, New York, 1991), Vol. 20, p.225.
- [44] R.A. Arndt, W.J. Briscoe, I.I. Strakovsky, and R.L. Workman, *Phys. Rev. C* **66**, 055213 (2002); M. Dugger et al. (CLAS Collaboration), *Phys. Rev. C* **76**, 025211 (2007).
- [45] T.-S.H. Lee, *Phys. Rev. Lett.* **50**, 157 (1983); *Phys. Rev. C* **29**, 195 (1984).
- [46] Review by H. Garcilazo and H.Mizutani,  *$\pi$ -NN System* (World Scientific, Singapore, 1990).
- [47] S.X. Nakamura, H. Kamano, and T. Ishikawa, *Phys. Rev. C* **96**, 042201(R) (2017).
- [48] B. Krusche et al., *Eur. Phys. J.* **A6**, 309 (1999).
- [49] U. Siodlaczek et al., *Eur. Phys. J.* **A10**, 365 (2001).
- [50] P. Benz et al. (Aachen-Bonn-Hamburg-Heidelberg-Muenchen Collaboration), *Nucl. Phys.* **B65**, 158 (1973).
- [51] CNS Data Analysis Center, George Washington University, <http://gwdac.phys.gwu.edu>
- [52] I. Blomqvist and J.M. Laget, *Nucl. Phys.* **A280**, 405 (1977).
- [53] J.M. Laget, *Nucl. Phys.* **A296**, 388 (1978).
- [54] J.M. Laget, *Phys. Rep.* **69**, 1 (1981).